J. Fluid Mech. (1997), *vol.* 335, *pp.* 361–392

Numerical simulation of the evolution of Tollmien–Schlichting waves over finite compliant panels

By CHRISTOPHER DAVIES[1] AND PETER W. CARPENTER[2]

[1]School of Mathematical and Information Sciences, Coventry University, Coventry, CV1 5FB, UK

[2]Department of Engineering, University of Warwick, Coventry, CV4 7AL, UK

(Received 8 June 1995 and in revised form 21 October 1996)

The evolution of two-dimensional Tollmien–Schlichting waves propagating along a wall shear layer as it passes over a compliant panel of finite length is investigated by means of numerical simulation. It is shown that the interaction of such waves with the edges of the panel can lead to complex patterns of behaviour. The behaviour of the Tollmien–Schlichting waves in this situation, particularly the effect on their growth rate, is pertinent to the practical application of compliant walls for the delay of laminar–turbulent transition. If compliant panels could be made sufficiently short whilst retaining the capability to stabilize Tollmien–Schlichting waves, there is a good prospect that multiple-panel compliant walls could be used to maintain laminar flow at indefinitely high Reynolds numbers.

We consider a model problem whereby a section of a plane channel is replaced with a compliant panel. A growing Tollmien–Schlichting wave is then introduced into the plane, rigid-walled, channel flow upstream of the compliant panel. The results obtained are very encouraging from the viewpoint of laminar-flow control. They indicate that compliant panels as short as a single Tollmien–Schlichting wavelength can have a strong stabilizing effect. In some cases the passage of the Tollmien–Schlichting wave over the panel edges leads to the excitation of stable flow-induced surface waves. The presence of these additional waves does not appear to be associated with any adverse effect on the stability of the Tollmien–Schlichting waves. Except very near the panel edges the panel response and flow perturbation can be represented by a superposition of the Tollmien–Schlichting wave and two other eigenmodes of the coupled Orr–Sommerfeld/compliant-wall eigensystem.

The numerical scheme employed for the simulations is derived from a novel vorticity–velocity formulation of the linearized Navier–Stokes equations and uses a mixed finite-difference/spectral spatial discretization. This approach facilitated the development of a highly efficient solution procedure. Problems with numerical stability were overcome by combining the inertias of the compliant wall and fluid when imposing the boundary conditions. This allowed the interactively coupled fluid and wall motions to be computed without any prior restriction on the form taken by the disturbances.

1. Introduction

The pursuit of a seemingly impossible goal motivated the present work. At first sight the prospects of using wall compliance to maintain laminar flow at indefinitely

high Reynolds number seem poor. In order to explain why this goal may be realizable by using suitably designed multiple-panel compliant walls it is necessary first to give some background information. This will also help to explain why the present work was undertaken.

In a low-disturbance environment, such as found in free flight and in some marine applications, quasi-two-dimensional Tollmien–Schlichting (TS) waves precede transition in the flat-plate boundary layer and similar flow fields. (See Schlichting 1979.) Various receptivity processes are responsible for generating these instabilities which are probably initially three-dimensional and randomly distributed. However, quasi-two-dimensional TS waves are preferentially amplified in the boundary layer. Further downstream the amplitude of the most amplified waves becomes sufficiently large for nonlinear effects to become important. Transition follows shortly thereafter. Evidently, then, if the growth of TS waves could be reduced or completely suppressed and providing that no other instability mechanism comes into play, transition could be postponed or even eliminated altogether.

It is now widely accepted that wall compliance can be used to stabilize TS waves. Carpenter & Morris (1990) carried out calculations of the growth of TS waves over the same type of compliant-wall model as used in the present work, indicating that about a fivefold rise in the transitional Reynolds number (Re_{xt}) is possible. Similar results for different types of compliant wall have also been obtained by Yeo (1988) and Dixon, Lucey & Carpenter (1994). Transition delays of this magnitude would lead to very useful drag reductions in many engineering applications, but are still a long way from maintaining laminar flow at indefinitely high Reynolds number. Moreover, further experimental verification is needed to make the theoretical predictions convincing. No experimental work has yet been done to verify the substantial transition delays predicted by the theory. Such experiments would be expensive and difficult. But the theory has been corroborated in a series of experiments by Gaster (1987) and his co-workers. These experiments were carried out with great care on a flat-plate model in a large towing tank. The plate was fitted with compliant panel inserts. The designs of the two-layer compliant walls were not in any way optimized for transition delay. Nevertheless, in some cases a very marked reduction was observed in the growth of TS waves for the compliant panels compared with the rigid surface. In the best case approximately a 30% increase in transitional Reynolds number was found. In fact, it was the limitations of the experimental set-up rather than the compliant-wall properties that made it impossible to achieve greater transition delays. The Gaster experiments were not designed with the intention of providing direct verification of transition delay. Their significance lies in the close agreement found between the measurements of TS wave growth and the corresponding theoretical predictions. Moreover, Lucey & Carpenter (1995) have recently demonstrated that there is also a close agreement between the theory and experimental observations for one of the wall-based modes found in flows over compliant walls. In fact, it is this instability – travelling-wave flutter – that appears to be the main route to transition for the boundary layers in the Gaster experiments. Most, if not all, of the features observed in these experiments can now be explained quantitatively on the basis of the appropriate linear stability theory. This gives us confidence in the reliability of the theory.

Carpenter & Morris based their approach, in part, on selecting wall properties for which the two main hydroelastic instabilities – travelling-wave flutter and divergence – were marginally stable. The estimate used for the onset speed of divergence was based on potential flow theory. This gives very conservative results, since it is known

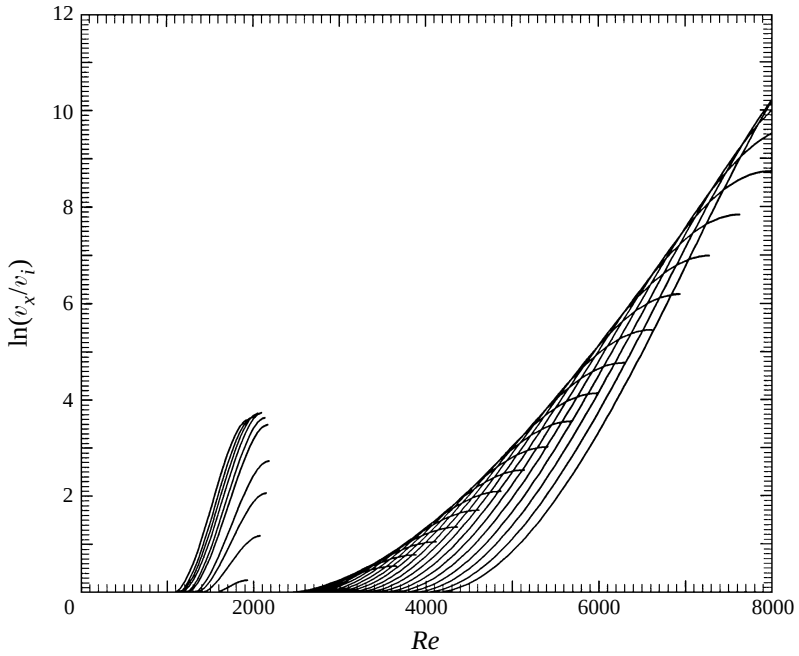

FIGURE 1. Theoretical amplification curves for a compliant wall with a good transition-delaying capability. Each curve corresponds to a fixed frequency with the magnitude falling from left to right. v_x and v_i denote respectively the amplitudes of the velocity perturbations at a streamwise station and at the point on the lower branch of the neutral curve corresponding to the fixed value of frequency.

(Kendall 1970 and Duncan, Waxman & Tulin 1985) that the presence of the boundary layer substantially reduces the fluctuating pressure at the wall compared with that found with purely potential flow. This effect is also evident in recent numerical simulations by Lucey, Cafolla & Carpenter (1997) for disturbances to a laminar boundary layer. The best estimates now available suggest that the divergence onset speed would be well in excess of twice the value assumed by Carpenter & Morris. In fact, it is only necessary to raise their value of the divergence onset speed by a factor of 1.4 to permit a choice of sets of wall properties that result in the complete suppression of TS waves over a range of Reynolds number. This is illustrated by the theoretical amplification curves plotted in figure 1 which were obtained using the methods of Carpenter & Morris. Each curve corresponds to a different value of TS frequency; the frequency falls as we move from left to right in the figure. The most noteworthy point about figure 1 is the complete suppression of the TS waves between approximately $Re_{\delta^*} = 2000$ and 2600 (where Re_{δ^*} is the local Reynolds number based on the boundary-layer displacement thickness). In figure 21 of Carpenter & Morris (1990) the same range of Reynolds number corresponds to a minimum in amplification, but complete suppression was not observed.

The range of Reynolds number corresponding to complete suppression can be changed at will by selecting different sets of wall properties. It thereby becomes clear that the wall properties could be locally tailored to achieve complete suppression of the TS waves. The best way to achieve this in practice would be to have a series of relatively short compliant panels each having properties to match its range of Reynolds numbers. This brings yet another advantage because small compliant panels are less vulnerable to hydroelastic instability than long ones (Lucey

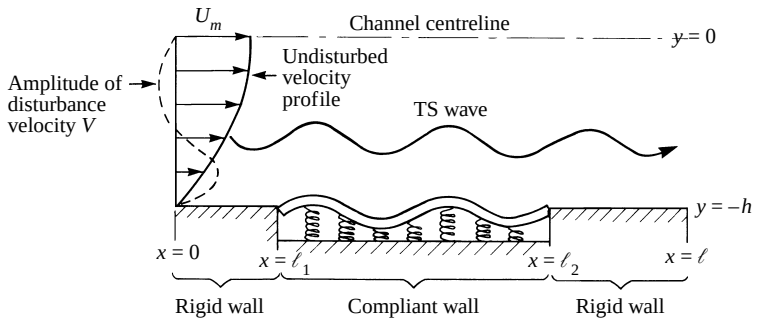

FIGURE 2. A schematic sketch of the problem under study. (It should be noted that the results of the simulations shown in subsequent figures correspond to the upper half of the channel.)

& Carpenter 1993*b*). Carpenter (1993) has shown that even the use of only two panels can lead to a substantial rise in the transition delay compared to a compliant wall having properties which are invariant in the streamwise direction. To be really effective at suppressing TS waves the theory suggests that we would want to use fairly small panels. But this theory is based on the assumption of infinitely long compliant walls. An obvious question is: Do panels as short as a few, or even one, TS wavelengths retain a capability to suppress TS waves? The present work was undertaken to provide an answer to this question.

We considered that for our purposes the best way to study the evolution of a TS wave in a wall shear flow over a finite compliant wall is by numerical simulation. In order to make the problem as simple as possible, while retaining all the essential features, we have studied a TS wave evolving in a fully developed two-dimensional channel flow (plane Poiseuille flow), rather than in a Blasius boundary layer. The channel flow has the advantage of being a truly parallel mean flow. We have also restricted the present numerical simulations to the linearized two-dimensional Navier–Stokes equations. We have already extended our methods to enable similar numerical simulations to be carried out for boundary layers. The resulting simulations in boundary-layer flow show that the essential physics is revealed by the present study. Accordingly, because of the attractions of keeping the extraneous flow details as simple as possible, we have chosen to undertake a comprehensive study using a channel flow as the basic undisturbed shear flow. It may also a more appropriate choice for the other possible applications of the work, briefly mentioned below.

The problem studied is illustrated in figure 2. The channel is fitted with a compliant insert between streamwise stations $x = \ell_1$ and $x = \ell_2$. The undisturbed velocity profile throughout is given by the well-known parabolic profile. At inlet ($x = 0$) the disturbance velocity is given by the appropriate TS eigenfunction of the Orr–Sommerfeld equation. At exit $x = \ell$ the solutions are required to be wave-like with the appropriate rigid-wall wavenumber, as determined by the Orr–Sommerfeld eigenvalue. Only symmetric disturbances (antisymmetric streamwise velocity) are considered. The compliant panel is modelled by the plate–spring model of Carpenter & Garrad (1985, 1986).

There are likely to be some interesting flow physics revealed by this type of numerical experiment. It is not just a question of observing the passage of a TS wave over the compliant panel. The panel itself can support waves independently of the TS wave. The TS wave may trigger other modes of response owing to scattering or reflection at the leading and trailing edges. Lucey & Carpenter (1993*a*) have shown

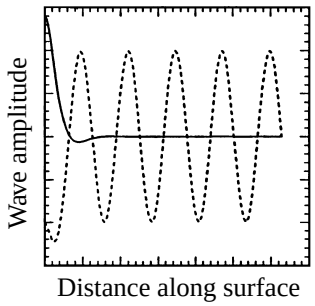

FIGURE 3. The variation of wall displacement for a plate-spring compliant panel driven harmonically in the absence of a fluid flow: ——, driver frequency below cut-off; and – – –, above cut-off.

that even for very long panels the leading and trailing edges exert a subtle effect on the phase of the wall displacement for these other modes over the whole of the panel. Thus the panel response may contain a range of wavenumbers in addition to that of the TS wave. Accordingly we may expect the spatial and temporal variations of such properties as wall displacement and pressure, and enstrophy and energy integrals to be highly complex.

The complexity of the panel's response is likely to be governed by whether the frequency of the TS wave is above or below cut-off. The cut-off phenomenon can be readily appreciated in the case where there is no flow and the panel is driven periodically at a point. In this case the cut-off frequency is given by $(K/m)^{1/2}$ where K and m are the spring stiffness and the areal density of the wall. A simple Green's function analysis similar to that found in Morse & Ingard (1968) leads to the results for wall displacement shown in figure 3. For this undamped wall it can be seen that only when the compliant panel is driven at a frequency above cut-off do waves propagate to infinity. For the present problem of a TS wave propagating over a panel we might expect to see a response dominated by the TS wave if its frequency is below the panel's cut-off frequency, but a much more complex response when this is not so. A further complicating factor is that with the presence of a fluid flow the definition and identification of the cut-off frequency is less straightforward.

Let us now turn briefly to the computational aspects of the work. Since fully nonlinear and three-dimensional direct numerical simulations are becoming almost commonplace, one may well expect the present linear two-dimensional simulations to be simple and straightforward. Certainly they require much less computer resources and the outlet boundary conditions are far less of a problem for linear simulations. There are, however, several special features of the current problem that make it a fairly challenging computational task requiring the development of special methods.

The evolution of TS waves and other disturbances in shear flow over a rigid wall is highly parabolic in character. Most direct numerical simulation techniques exploit this feature either explicitly or implicitly. The recently developed and highly efficient parabolic-stability-equation (PSE) approach due to Bertolotti, Herbert & Spalart (1992) is obviously based on the usual parabolic nature of disturbance evolution. It cannot be used for the present problem. Many successful direct numerical simulations are so-called temporal simulations based on spectral codes with periodic boundary conditions. Examples are the numerical simulations of instabilities developing in boundary layers (Wray & Hussaini 1984), in fully developed plane channel flow

(Gilbert & Kleiser 1986) and in boundary layers over compliant walls (Domaradzki & Metcalfe 1987 and Metcalfe *et al.* 1991). This type of approach depends on a close analogy existing between the true spatially developing flow field and a model, purely temporally evolving, one. This crucial analogy only remains valid if the parabolic character of the disturbance evolution is preserved. For the present problem where strong upstream influence is anticipated only a truly spatial simulation will meet the requirements. Accordingly our approach follows in part the work of Fasel and his co-workers (Fasel 1976; Fasel & Konzelmann 1990; Fasel, Rist & Konzelmann 1990).

Perhaps, the main difficulty encountered in the present work is associated with the need to simulate interactive coupling between the fluid flow and the compliant wall: the fluid flow generates forces which drive the wall while the resulting wall motion strongly influences the flow field. This state of affairs makes it difficult to achieve a stable iterative scheme. Domaradzki & Metcalfe (1987) and Metcalfe *et al.* (1991) successfully overcame these problems but, for the reasons set out above, their temporal-simulation approach will not work for the present problem. It is easier to achieve a stable scheme if the inertia of the wall is neglected, as in the recent scheme due to Luo & Pedley (1996). A stable scheme can also be achieved relatively easily if it is assumed that the solutions are fully periodic in time. This allows us to replace time derivatives of the quantity Q by $\mathrm{i}\omega Q$ where ω is the disturbance frequency. Our early simulations were based on this approach (see Davies 1995). In some cases this approach produces satisfactory simulations. But it is not really acceptable in a numerical experiment to make this assumption *a priori* and, in fact, it turns out to be invalid for many cases of interest.

Lucey & Carpenter (1992) provide guidance on how a stable iterative scheme may be developed. They highlighted the need to combine terms representing the wall and hydrodynamic inertias. Belanger *et al.* (1994) have also followed a similar procedure in their recent simulations of flow–structure interaction. The reason for proceeding in the way developed by Lucey & Carpenter can be roughly explained as follows. If the inertia terms are treated separately, so that they lie on opposite sides of the equation used in the iterative scheme, there is always the danger that one of the two terms will dominate the other causing the iterative scheme to fail to converge. In our scheme we achieve the same end by notionally treating the total normal momentum of the system (flow plus wall) as a single variable.

Our overall objective for the numerical aspects of the work was to develop a highly efficient scheme which is capable of resolving all the features of the flow field and could achieve stable converged solutions even for non-periodic temporal variation. To this end we have developed a hybrid spectral/finite-difference approach based on a novel velocity–vorticity formulation which results in a very efficient and stable tridiagonal scheme.

At this point we will briefly mention other possible applications of the present work. It might well be expected to be of some relevance to certain problems in biomechanics. The literature for this subject is vast, so we will confine ourselves to referencing some recent reviews (Kamm 1987; Skalak, Özkaya & Skalak 1989; Grotberg 1994) and a few selected recent papers. There seems little evidence that TS waves themselves are relevant to any biomechanical phenomenon. However, the numerical methods developed for the present work and some aspects of the physics may well be applicable. For example, rigid inserts (stents) are sometimes used to reinforce blood vessels in the treatment of cardiovascular disease. Recent numerical simulations by Henry & Collins (1996) of arterial flows with rigid/compliant joins in the wall show some aspects of the flow physics revealed by our simulations. Another

example is the the phenomenon of collapsible tubes which has received considerable attention recently – fairly recent reviews are given by Kamm (1987) and Kamm & Pedley (1989). More recently Pedley and his co-workers (Rast 1994, Luo and Pedley 1995, 1996 and others) have carried out a number of related numerical simulations for a two-dimensional channel flow with a membrane of finite length replacing part of one of the otherwise rigid walls. These simulations have been carried out to investigate a new mechanism for the collapse of elastic tubes which was proposed by Pedley (1992).

The remainder of the paper is set out as follows. The formulation of the problem is discussed in §2. The numerical methods are discussed in §3. Sections 3.1 and 3.2 describe the methods used to discretize the fluid flow and wall motion respectively. Section 3.2 also describes how the wall and fluid inertias are combined to obtain a stable iterative scheme. Code validation is briefly discussed in §3.3. The main results of the numerical experiments are presented and discussed in §4. The results for TS frequency below cut-off are presented in §4.1. An analysis of the energy flux terms is given in §4.2. An approximate representation of the wall response is developed in §4.3 and the effect of the fluid flow on the cut-off frequency is discussed. Results for TS frequency above cut-off are presented in §4.4. Some additional simulations are briefly described in §4.5. Finally conclusions follow in §5.

2. Formulation of the mathematical problem

The mathematical problem is depicted in figure 2. The computational domain corresponds to a portion of a fully developed plane channel flow. A Tollmien–Schlichting wave enters the domain at $x = 0$. Unless stated otherwise all quantities are non-dimensional with the channel half-width h, flow speed U_m along the centreline and fluid density ρ, used as reference. (Hereafter ℓ denotes a dimensionless length.) Thus the domain is defined as $0 \leqslant x \leqslant \ell$ and $-1 \leqslant y \leqslant 1$. The channel wall is fitted with a compliant panel between $x = \ell_1$ and $x = \ell_2$, elsewhere it is rigid. We have restricted attention to normal disturbance velocity components, v, which are symmetrical (implying antisymmetrical streamwise disturbance velocity, u, and symmetrical vorticity disturbance, ω), because disturbances of this type determine the stability in the case of rigid walls (Drazin & Reid 1981).

Our vorticity–velocity formulation of the linearized two-dimensional Navier–Stokes equations takes the form

$$\frac{\partial \omega}{\partial t} + U\frac{\partial \omega}{\partial x} + U'' v = \frac{1}{R}\nabla^2 \omega, \tag{2.1a}$$

$$u = \int_0^y \omega \mathrm{d}y + \frac{\partial}{\partial x}\int_0^y v \mathrm{d}y; \qquad \nabla^2 v = -\frac{\partial \omega}{\partial x}, \tag{2.1b,c}$$

where the undisturbed flow speed $U = 1 - y^2$ and R is the Reynolds number based on h and U_m. Equation (2.1a) is the vorticity transport equation and (2.1b) has been derived from the definition of vorticity, namely

$$\omega = \frac{\partial u}{\partial y} - \frac{\partial v}{\partial x}.$$

Equation (2.1a) is decoupled from u, so that as matters stand the problem would be ill-posed because the evolution of the vorticity disturbance would not be influenced by the boundary conditions imposed on u (this problem would not occur if nonlinear terms were included). This is remedied by deriving an integral constraint on ω from

(2.1*b*) which takes the form

$$\int_0^1 \omega \mathrm{d}y = u_w - \frac{\partial}{\partial x}\int_0^1 v \mathrm{d}y \tag{2.2}$$

where suffix w denotes evaluation at the wall.

The use of (2.1*b*) and (2.1*c*), together with the symmetry condition, ensures that the incompressiblity condition

$$\mathscr{D} \equiv \frac{\partial u}{\partial x} + \frac{\partial v}{\partial y} = 0$$

is satisfied throughout the domain.

The merits of using a vorticity–velocity approach for spatial simulations of stability and transition are discussed by Fasel (1980). A more general review discussing the merits and demerits of the approach is given by Gatski (1991). Our vorticity–velocity formulation is significantly different from the usual approach and it is worth discussing the reasons for this. Usually a second Poisson equation of the form

$$\nabla^2 u = \frac{\partial \omega}{\partial y} \tag{2.3}$$

is used instead of (2.1*b*). There is a general difficulty with the use of the set of equations (2.1*a*, *c*) and (2.3) in that they only imply $\nabla^2 \mathscr{D} = 0$ rather than $\mathscr{D} = 0$. But from the maximal principle of harmonic functions it follows that if $\mathscr{D} = 0$ on the boundary, it will hold everywhere in the interior of the domain. Accordingly Fasel (1980) chose to use a discretized version of $\mathscr{D} = 0$ applied at the wall in developing his finite-difference representation for $(\partial^2 v/\partial y^2)_w$. It is not clear that this procedure can be formally justified, although it gives acceptable results in practice. It would appear that mathematically our procedure is more satisfactory.

At $x = 0$ the inlet boundary conditions are supplied by the real part of the appropriate Orr–Sommerfeld eigensolutions for v and ω. No inlet boundary condition is required for u. For the outlet condition at $x = \ell$ we follow Fasel (1976) and require the flow variables to be wave-like, i.e. $\sim \exp(\mathrm{i}\alpha_r x)$, at outlet, so that

$$\frac{\partial^2 v}{\partial x^2} + \alpha_r^2 v = 0, \qquad \frac{\partial^2 \omega}{\partial x^2} + \alpha_r^2 \omega = 0. \tag{2.4a, b}$$

He found that this type of boundary condition allowed small-amplitude two-dimensional TS waves to pass smoothly out of the computational domain. Kloker, Konzelmann & Fasel (1993) have studied the effects of the outflow boundary conditions in transition simulations. From their work it appears that problems may be encountered with the present approach when nonlinear terms are included in the governing equations and the wave amplitudes are larger. For the present linear calculations α was chosen to be the appropriate Orr–Sommerfeld eigenvalue. In some cases advantage could be gained by using the imaginary part of the eigenvalue to specify a growing wave at outlet. No problems were encountered in using the boundary conditions (2.4) when the rigid outlet portion of the wall was varied in length, even in the case when the wall was compliant at outlet.

The plate–spring model of Carpenter & Garrad (1985) is used for the dynamics of the compliant wall which is, accordingly, governed by the following equation:

$$m\frac{\partial^2 \eta}{\partial t^2} + \frac{d}{R}\frac{\partial \eta}{\partial t} + \frac{1}{R^2}\left(B\frac{\partial^4}{\partial x^4} - T\frac{\partial^2}{\partial x^2} + K\right)\eta = p_w \tag{2.5}$$

where η is the dimensionless vertical wall displacement (horizontal displacements are neglected in this model), p_w is the dimensionless hydrodynamic pressure disturbance acting on the wall; m, d, B, T and K are all non-dimensional wall parameters and are respectively the areal density, damping coefficient, flexural rigidity, applied streamwise tension per unit span and spring stiffness per unit area of the compliant wall. It is inconvenient to make the wall parameters dimensionless using U_m as a reference quantity, since the wall parameters will change when the centreline flow speed is altered during a series of computational experiments. To remove this difficulty the kinematic viscosity, ν, has been used as a reference quantity instead of U_m. This has the effect of introducing the factors involving R in (2.5). Thus using an asterisk to denote a dimensional quantity we have

$$m \equiv \frac{m^*}{\rho h}, \qquad \frac{d^*}{\rho U_m} = \frac{1}{R}\underbrace{\frac{d^*\rho h}{\nu}}_{d}, \qquad \frac{B^*}{\rho h^3 U_m^2} = \frac{1}{R^2}\underbrace{\frac{B^*}{\rho h \nu^2}}_{B},$$

$$\frac{T^*}{\rho h U_m^2} = \frac{1}{R^2}\underbrace{\frac{T^* h}{\rho \nu^2}}_{T}, \qquad \frac{K^* h}{\rho U_m^2} = \frac{1}{R^2}\underbrace{\frac{K^* h^3}{\rho \nu^2}}_{K}.$$

At the panel edges $x = \ell_1$ and $x = \ell_2$ we have imposed hinged conditions, i.e.

$$\eta = \frac{\partial^2 \eta}{\partial x^2} = 0 \qquad \text{at} \qquad x = \ell_1 \qquad \text{and} \qquad x = \ell_2. \tag{2.6}$$

Owing to the sudden change in surface slope hinged conditions are more demanding computationally than clamped ends and, for this reason, most of the simulations reported used conditions (2.6). Some simulations using clamped end conditions will be briefly reported in §4.5.

At the wall the boundary conditions $u = v = 0$ are applied for the rigid-wall portion $0 \leqslant x \leqslant \ell_1$ and $\ell_2 \leqslant x \leqslant \ell$. At the compliant wall the velocity and stress components are continuous between fluid and solid. Thus when linearized the boundary conditions on velocity become

$$u_w = -U_w' \eta, \qquad v_w = \frac{\partial \eta}{\partial t}. \tag{2.7a, b}$$

The pressure disturbance can be obtained by integrating the linearized y-momentum equation of the Navier–Stokes equations:

$$p = -\int_0^y \left(\frac{\partial v}{\partial t} + U\frac{\partial v}{\partial x} + \frac{1}{R}\frac{\partial \omega}{\partial x} \right) \mathrm{d}y. \tag{2.8}$$

In practice the term involving the factor $1/R$ is negligible. The driving pressure term on the right-hand side of (2.5) is obtained from (2.8) by setting $y = 1$.

At this point it should be noted that there is also a mean pressure gradient along a horizontal plane channel flow. Physically this would produce a small mean wall deflection and thereby a small change to the mean flow. This may produce extraneous effects which would obscure the interaction of the TS wave with the leading and trailing edges of the compliant panel. Since the investigation of this interaction is the main aim of the present work we will assume that the mean pressure has equilibriated on either side of the plate, allowing its effect on the wall displacement to be neglected. Alternatively the channel could be assumed to be inclined to the horizontal, thereby eliminating the streamwise pressure gradient. But, in any case, the mean pressure gradient is only $O(1/R)$, so its effect is relatively minor.

In cases where the wall is still compliant at outlet, i.e. $\ell_2 = \ell$, a wave-like outlet boundary condition analogous to (2.4a, b) can be derived for the wall displacement η (Davies 1995).

3. Numerical methods

3.1. *Fluid flow*

The numerical scheme is based on a spectral Chebyshev tau treatment of the variations in the y-direction combined with second-order finite-difference discretization for the temporal and streamwise spatial variations. The advantages of using a spectral scheme in the y-direction are that it can accurately resolve the disturbance profile and accurately evaluate the pressure integral (2.8) which is crucial for this interactive simulation. In fact, as will be seen below, we have been able to construct a tridiagonal scheme, so that the increased resolution of the spectral method is obtained without any significant penalty in computing time.

3.1.1. *Spectral scheme for y-variations*

The vorticity and normal-velocity disturbances are expanded in even Chebyshev polynomials as follows:

$$\omega(x, y, t) = \tfrac{1}{2}\omega_1(x, t) + \sum_{k=2}^{N} \omega_k(x, t) T_{2(k-1)}(y), \tag{3.1}$$

$$v(x, y, t) = \tfrac{1}{2}v_1(x, t) + \sum_{k=2}^{N} v_k(x, t) T_{2(k-1)}(y), \tag{3.2}$$

where T_n is the nth Chebyshev polynomial. Only even polynomials are used because we are restricting attention to even disturbance modes. An expansion for u would comprise odd polynomials, but there is no need to solve for u directly; it can be obtained from (2.1b) once ω and v are known.

Following the treatment of the Orr–Sommerfeld equation by Bridges & Morris (1984) we have found that integral operators lead to a more convenient form of spectral expansion than differential operators. Accordingly (2.1a, c) are integrated twice to obtain

$$\frac{\partial}{\partial t}\int\int \omega + \frac{\partial}{\partial x}\int\int U\omega + \int\int U'' v = \frac{1}{R}\left(\omega + \frac{\partial^2}{\partial x^2}\int\int \omega\right) + c(x, t), \tag{3.3}$$

$$v + \frac{\partial^2}{\partial x^2}\int\int v = -\frac{\partial}{\partial x}\int\int \omega + d(x, t), \tag{3.4}$$

where

$$\int\int \omega \quad \text{etc.} \qquad \text{denotes} \qquad \int_0^y \int_0^{y'} \omega(y'')\,\mathrm{d}y''\,\mathrm{d}y' \quad \text{etc.}$$

and $c(x, t)$ and $d(x, t)$ are integration functions.

Substitution of (3.1) and (3.2) into (3.3) and (3.4) leads to the two systems of equations

$$I_{jk}\left(\frac{\partial \omega_k}{\partial t} - 2v_k - \frac{1}{R}\frac{\partial^2 \omega_k}{\partial x^2}\right) - \frac{1}{R}\omega_j + U_{jk}\frac{\partial \omega_k}{\partial x} = 0, \tag{3.5}$$

$$v_j + I_{jk}\left(\frac{\partial^2 v_k}{\partial x^2} + \frac{\partial \omega_k}{\partial x}\right) = 0, \tag{3.6}$$

for $j = 2, ..., N$. Here and elsewhere we use the repeated-suffix convention to imply summation over k from 1 to N. Using f to denote an arbitrary variable, the matrix operator I_{jk} is equivalent to $\int\int f$ and is defined as

$$I_{jk}f_k = \frac{\delta_{jk}}{8}\left(\frac{f_{k-1}}{(k-1)(2k-3)} - \frac{4f_k}{(2k-1)(2k-3)} + \frac{f_{k-1}}{(k-1)(2k-1)}\right). \tag{3.7}$$

The matrix operator U_{jk} represents $\int\int Uf$. The parabolic mean velocity leads to a pentadiagonal form. The jth equation in each of (3.5) and (3.6) has been obtained by equating coefficients of $T_{2(j-1)}$. The operators also generate the higher-order polynomials T_{2N} and $T_{2(N+1)}$. Following the usual practice with a tau-method (Canuto *et al.* 1988) we do not attempt to match the coefficients of these polynomials. The $j = 1$ equations have been deliberately omitted because they involve the unknown integration functions c and d. A total of $2N$ equations for the $2N$ coefficients of ω_k and v_k are obtained by replacing these omitted equations by two other equations derived from the integral and boundary conditions (2.2) and (2.7*b*). These are given by

$$q_k\left(\omega_k + \frac{\partial v_k}{\partial x}\right) = u_w, \qquad r_k v_k = v_w, \tag{3.8a, b}$$

where

$$q_1 = r_1 = \tfrac{1}{2}, \qquad q_{k+1} = \int_0^1 T_{2k}(y)\mathrm{d}y = -\frac{1}{4k^2-1}, \qquad r_{k+1} = T_{2k}(1) = 1.$$

Given v_k, (3.8*a*) and (3.5) could be solved for ω_k; equally, given ω_k, (3.6) and (3.8*b*) could be solved for v_k. This indicates the basis of the interation scheme which is incorporated into the marching scheme used to determine the streamwise variation.

3.1.2. *Finite-difference schemes for temporal and spatial variations*

Initially the Crank–Nicholson method was tried for discretizing the time derivative. It failed in many cases and, accordingly, was abandoned in favour of a fully implicit three-point backward-difference method. Centred differences are used for all x-derivatives. In both cases second-order schemes are used. Implicit time discretization is necessary to obtain numerical stability when resolving unsteady disturbances in a viscous flow at high Reynolds numbers (Fasel 1980). The type of interactive problem studied herein is even more difficult in this regard; implicit methods have proved to be absolutely neccesary even when potential flow is used to model the fluid dynamics (Lucey & Carpenter 1992).

Using the notation

$$f^{\ell}_{k,n} = f_k(x_n, t_\ell)$$

the three-point implicit time discretization takes the form

$$\left(\frac{\partial f_{k,n}}{\partial t}\right)^{\ell} = \frac{1}{2\Delta t}\left(3f^{\ell}_{k,n} - 4f^{\ell-1}_{k,n} + f^{\ell-2}_{k,n}\right)$$

and the system of equations (3.5), (3.6), (3.8a,b) becomes

$$\left\{I_{jk}\left(3 + \frac{4\Delta t}{R(\Delta x)^2}\right) - 2\delta_{jk}\frac{\Delta t}{R}\right\}\omega^{\ell}_{k,n} + U_{jk}\frac{\Delta t}{\Delta x}\left(\omega^{\ell}_{k,n+1} - \omega^{\ell}_{k,n-1}\right)$$
$$-I_{jk}\left(4\omega^{\ell-1}_{k,n} - \omega^{\ell-2}_{k,n} + 4\Delta t v^{\ell}_{k,n} + \frac{2\Delta t}{R(\Delta x)^2}\left(\omega^{\ell}_{k,n+1} + \omega^{\ell}_{k,n-1}\right)\right) = 0, \tag{3.9}$$

$$\left(2I_{jk} - (\Delta x)^2\delta_{jk}\right) v^{\ell}_{k,n} - I_{jk}\left(v^{\ell}_{k,n+1} + v^{\ell}_{k,n-1} + \tfrac{1}{2}\Delta x\left(\omega^{\ell}_{k,n+1} - \omega^{\ell}_{k,n-1}\right)\right) = 0, \qquad (3.10)$$

$$q_k\left(\omega^{\ell}_{k,n} + \frac{1}{2\Delta x}(v^{\ell}_{k,n+1} - v^{\ell}_{k,n-1})\right) = (u_w)^{\ell}_n, \qquad \tilde{r}_k v^{\ell}_{k,n} = \tilde{v}^{\ell}_n, \qquad (3.11a,b)$$

where Δx and Δt are respectively the steps in x and t. The repeated suffix convention holds for j also, except that the $j = 1$ equation is omitted in (3.9) and (3.10). For the time being $\tilde{r}_k$ and $\tilde{v}$ can be indentified with r_k and v_w respectively. In §3.3 it will be shown how they need to be replaced by generalized expressions in order to obtain a stable convergent iterative procedure.

The pairs of equations (3.9) and (3.11a) and (3.10) and (3.11b) can be combined to form two matrix equations of the forms

$$\boldsymbol{S}\boldsymbol{\Omega}^{\ell}_n = \boldsymbol{L}\left(\boldsymbol{V}^{\ell}_n, \boldsymbol{\Omega}^{\ell}_{n+1}, \boldsymbol{\Omega}^{\ell}_{n-1}, \boldsymbol{\Omega}^{\ell-1}_n, \boldsymbol{\Omega}^{\ell-2}_n; (u_w)^{\ell}_n, \boldsymbol{V}^{\ell}_{n+1}, \boldsymbol{V}^{\ell}_{n-1}\right), \qquad (3.12)$$

$$\boldsymbol{T}\boldsymbol{V}^{\ell}_n = \boldsymbol{M}\left(\boldsymbol{V}^{\ell}_{n+1}, \boldsymbol{V}^{\ell}_{n-1}, \boldsymbol{\Omega}^{\ell}_{n+1}, \boldsymbol{\Omega}^{\ell}_{n-1}; \tilde{v}^{\ell}_n\right), \qquad (3.13)$$

where $\boldsymbol{\Omega}^{\ell}_n$ and $\boldsymbol{V}^{\ell}_n$ are vectors of Chebyshev coefficients and the matrices $\boldsymbol{S}$ and $\boldsymbol{T}$ are given by

$$S_{jk} = \begin{cases} -\dfrac{1}{4(k-1)^2 - 1}\left(1 - \tfrac{1}{2}\delta_{1k}\right) & \text{if } j = 1 \\ I_{jk}\left(3 + \dfrac{4\Delta t}{R(\Delta x)^2}\right) - 2\delta_{jk}\dfrac{\Delta t}{R} & \text{otherwise.} \end{cases}$$

$$T_{jk} = \begin{cases} 1 - \tfrac{1}{2}\delta_{1k} & \text{if } j = 1 \\ 2I_{jk} - (\Delta x)^2\delta_{jk} & \text{otherwise.} \end{cases}$$

The detailed structure of the vector operators $\boldsymbol{L}$ and $\boldsymbol{M}$ can be determined from (3.9), (3.10) and (3.11a,b).

The quantities after the semi-colon in the arguments of $\boldsymbol{L}$ and $\boldsymbol{M}$ only affect the values of the first components. Hence it follows from the tridiagonal form of I_{jk} that, apart from their first rows, the matrices $\boldsymbol{S}$ and $\boldsymbol{T}$ are tridiagonal in form.

The system of equations (3.12) and (3.13) define a line iteration process. For incremental downstream locations the Chebyshev vectors are recalculated. Updated values are then immediately used in the calculations at the next streamwise position. When the outflow boundary is reached and the Chebyshev vectors recalculated there, the whole process is repeated, beginning at the inlet, until convergence is achieved. This streamwise marching procedure is similar to that used by Fasel (1976).

3.1.3. *Boundary conditions*

At inlet ($n = 0$)

$$\boldsymbol{V}^{\ell}_0 = \mathscr{R}\left(\boldsymbol{V}_{OS}\mathrm{e}^{-\mathrm{i}\beta\ell\Delta t}\right), \qquad \boldsymbol{\Omega}^{\ell}_0 = \mathscr{R}\left(\boldsymbol{\Omega}_{OS}\mathrm{e}^{-\mathrm{i}\beta\ell\Delta t}\right).$$

The corresponding vectors of Chebyshev coefficients are obtained from numerical solution of the Orr–Sommerfeld equation.

The boundary conditions at the outflow ($n = n_e$) follow from (2.4a,b):

$$\boldsymbol{V}^{\ell}_{n_e+1} = \left(2 - \alpha_r^2(\Delta x)^2\right)\boldsymbol{V}^{\ell}_{n_e} - \boldsymbol{V}^{\ell}_{n_e-1}, \qquad \boldsymbol{\Omega}^{\ell}_{n_e+1} = \left(2 - \alpha_r^2(\Delta x)^2\right)\boldsymbol{\Omega}^{\ell}_{n_e} - \boldsymbol{\Omega}^{\ell}_{n_e-1}.$$

Here we have introduced dummy grid points outside the domain at $n = n_e + 1$. The values at $n = n_e$ are updated in exactly the same way as for interior points using (3.12) and (3.13). Afterwards the outflow boundary conditions are used to update values at $n = n_e + 1$.

Owing to their predominantly tridiagonal form the matrix equations (3.12) and (3.13) can be solved using a modified Thomas algorithm, the details of which are given in Davies (1995).

3.2. *Wall motion*

Values of $(u_w)_n^\ell$ and $(v_w)_n^\ell$ (retaining for the time being the identity between $\tilde{v}$ and v_w) must be supplied in order to solve the system of equations (3.12) and (3.13) for the fluid flow. From updated values of the vectors of Chebyshev coefficients, $\boldsymbol{V}$ and $\boldsymbol{\Omega}$, p_w could be recalculated from the discretized form of (2.8). This could then be used in a discretized form of the wall equation (2.5) to solve for wall displacements and velocities leading to new values for $(u_w)_n^\ell$ and $(v_w)_n^\ell$. One might well imagine this process could form the basis of an iterative procedure. However, any attempt to implement such a scheme based on a straightforward discretization of the equation (2.5) for the wall motion and on identifying $\tilde{v}$ with v_w would usually lead to numerical instability and a failure to converge. As noted in §1, in order to obtain a stable scheme it is necessary to follow Lucey & Carpenter (1992) in grouping the wall and hydrodynamic inertias together. Otherwise, if treated separately, one or the other may dominate causing the iteration to fail to converge. In the present context this can be achieved by notionally treating the total normal momentum of the channel as a single variable:

$$\mu = mv_w + \int_0^1 v\,\mathrm{d}y. \tag{3.14}$$

Thus, using (2.8) for p_w, the wall equation (2.5) can be rewritten as

$$\frac{\partial \mu}{\partial t} + \frac{1}{R^2}\left(B\frac{\partial^4}{\partial x^4} - T\frac{\partial^2}{\partial x^2} + K\right)\eta + \frac{d}{R}v_w = -\frac{\partial}{\partial x}\int_0^1 \left(Uv + \frac{1}{R}\omega\right)\mathrm{d}y. \tag{3.15}$$

The wall boundary condition (2.7*b*) needs to be replaced by a boundary condition on μ. This new boundary condition can be obtained by applying the three-point backward difference scheme from §3.1 to discretize the time derivative of μ appearing in (3.15). In the same way the boundary condition (2.7*b*) becomes

$$\eta^\ell = \tfrac{1}{3}\left(4\eta^{\ell-1} - \eta^{\ell-2}\right) + \tfrac{2}{3}\Delta t (v_w)^\ell. \tag{3.16}$$

Equation (3.16) can be used to eliminate η^ℓ from the discretized form of (3.15). We thereby arrive at the required boundary condition on μ, namely

$$\mu^\ell + \left(\frac{2d\Delta t}{3R} + \frac{4(\Delta t)^2}{9}\mathscr{K}\right)v_w^\ell = \tfrac{1}{3}\left(4\mu^{\ell-1} - \mu^{\ell-2}\right) - \frac{2\Delta t}{9}\left(4\mathscr{K}\eta^{\ell-1} - \mathscr{K}\eta^{\ell-2}\right) - \tfrac{2}{3}\Delta t\frac{\partial}{\partial x}\int_0^1 \left(Uv^\ell + \frac{1}{R}\omega^\ell\right)\mathrm{d}y, \tag{3.17}$$

where

$$\mathscr{K} \equiv \frac{1}{R^2}\left(B\frac{\partial^4}{\partial x^4} - T\frac{\partial^2}{\partial x^2} + K\right).$$

The streamwise derivatives may be discretized using second-order finite differences and the Chebyshev expansions (3.1) and (3.2) used for v and ω. Direct reference to μ can then be eliminated by reverting to writing it in the form on the right-hand side of (3.14). In this way the final version of the new boundary condition is obtained in the following form:

$$\tilde{r}_k v_k = \tilde{v}, \tag{3.18}$$

where

$$\tilde{r}_k = \left(m + \frac{2d\Delta t}{3R} + \frac{4(\Delta t)^2}{9}K_0\right) r_k + q_k,$$

$$\tilde{v} = \tfrac{1}{3}(mr_k + q_k)\left(4v_{k,n}^{\ell-1} - v_{k,n}^{\ell-2}\right) - \frac{2\Delta t}{9}\left(4(\mathscr{K}\eta)_n^{\ell-1} - (\mathscr{K}\eta)_n^{\ell-2}\right)$$
$$-\frac{\Delta t}{3\Delta x}\left(s_k\left(v_{k,n+1}^{\ell} - v_{k,n-1}^{\ell}\right) + \frac{1}{R}q_k\left(\omega_{k,n+1}^{\ell} - \omega_{k,n-1}^{\ell}\right)\right)$$
$$+\frac{4(\Delta t)^t}{9}r_k\left(K_1\left(v_{k,n+1}^{\ell} + v_{k,n-1}^{\ell}\right) - K_2\left(v_{k,n+2}^{\ell} + v_{k,n-2}^{\ell}\right)\right),$$

$$K_0 = \frac{1}{R^2}\left(\frac{6B}{(\Delta x)^4} + \frac{2T}{(\Delta x)^2} + K\right), \quad K_1 = \frac{1}{R^2}\left(\frac{4B}{(\Delta x)^4} + \frac{T}{(\Delta x)^2}\right), \quad K_2 = \frac{1}{R^2}\frac{B}{(\Delta x)^4}.$$

Full details of the derivation of (3.17) and (3.18) may be found in Davies (1995).

The values of $\tilde{v}$ at successive streamwise positions need to be recalculated using the latest available estimates for v and ω. Thus

$$\tilde{v}_n^{\ell,i} = \tilde{v}\left(\boldsymbol{V}_n^{\ell-1}, \boldsymbol{V}_n^{\ell-2}, \mathscr{K}\eta_n^{\ell-1}, \mathscr{K}\eta_n^{\ell-2}, \boldsymbol{V}_{n-1}^{\ell,i}, \boldsymbol{V}_{n+1}^{\ell,i-1}, \omega_{n-1}^{\ell,i}, \omega_{n+1}^{\ell,i-1}\right). \tag{3.19}$$

The details of the functional dependence follow from the definition of $\tilde{v}$ given above.

The new boundary condition (3.18) now replaces (3.11b) and the matrix operator $\boldsymbol{T}$ and matrix $\boldsymbol{M}$ in (3.13) are modified accordingly. Thus with use of (3.19) to determine $\tilde{v}^{\ell,i}$ the updated value of $\boldsymbol{V}_n^{\ell,i}$ can be calculated by solving the amended version of (3.13). The rigid-wall boundary condition can be accommodated within the same framework by requiring

$$\tilde{v}_n^{\ell,i} = \int_0^1 v_n^{\ell,i-1}\mathrm{d}y = q_k v_{k,n}^{\ell,i-1}. \tag{3.20}$$

In conjunction with (3.18) this ensures that the condition $v_w = 0$ is satisfied when the iteration converges. By imposing the boundary condition in this way we avoid the need to make further changes to the line iteration matrix $\boldsymbol{T}$ when dealing with the rigid-walled section of the channel.

It remains to describe the method used to determine the values of the wall displacement η^{ℓ} which must be inserted into the boundary condition (2.7a) for u_w. Two distinct methods have been validated. The first employs the governing equation (3.15) to obtain a block-tridiagonal system of equations. This can be efficiently solved for η^{ℓ} when the most recently updated values of v and ω are supplied. Further details are given in Davies (1995). The second method has been developed more recently. It uses the relation (3.16) to determine η^{ℓ} directly. Such an approach is made possible by the removal of all reference to η^{ℓ} from the boundary condition (3.18) applied to v. Both methods of determining η^{ℓ} proved to be effective for the numerical simulations, but the second method, which uses (3.16) in a simple manner, appears to be more efficient, converged solutions being obtained after fewer iterations.

In summary, then, the single-loop iterative procedure is as follows:

(i) Flow-field variables ω and v are updated through a streamwise marching process by solving (3.12) and (3.13). In (3.12) the previous values of u_w can be used, but the function $\tilde{v}$ must be recalculated within the streamwise marching procedure.

(ii) Equation (3.16) is then used to obtain updated values of the wall displacement η.

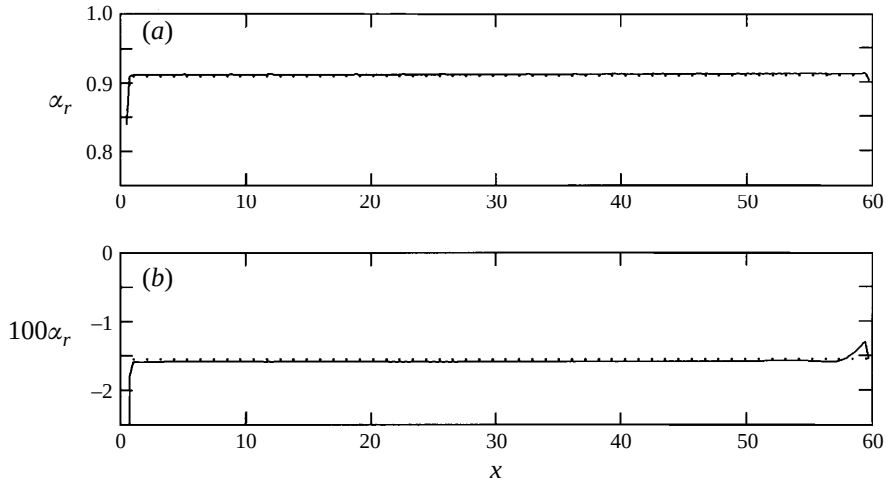

FIGURE 4. Streamwise variation of (*a*) locally defined wavenumber and (*b*) spatial growth rate for a TS wave propagating along a rigid-walled channel. $R = 12\,000$ and dimensionless frequency, $\beta = 0.2$. —, The results of the numerical simulation; ····, the predictions of conventional linear stability theory. (Data are displayed for the whole length of the domain used in the simulation.)

(iii) Updated values of u_w can now be obtained from (2.7*a*) and passed back to the fluid-flow update routine in (i).

The whole process is repeated until a converged solution is found. The same iterative procedure needs to be applied at each time step.

3.3. *Code validation*

The two obvious tests of the computer code are to check whether it can produce the correct results when the channel wall is either wholly rigid or wholly compliant. Tests of this kind were carried out satisfactorily. These simulations were carried out by using null values to initialize the disturbance field and then introducing the time-periodic forcing appropriate to the expected TS eigenmode at the inlet. For testing purposes we used results corresponding to a time after the leading front of the disturbance, generated in this way, has propagated out of the downstream boundary of the computational domain. No reflections of the disturbance at the outlet occurred. Experimentation, using different values for the wavenumber in the implementation of the outflow boundary condition, showed that there is a fair degree of insensitivity to the precise value of α_r chosen. This was to be expected from the previous studies of Fasel (1976).

Good agreement was found generally between the linear theory and the simulation results. A fairly stringent test is to compare wavenumbers and spatial growth rates. This is done in figure 4. As can be seen there is excellent agreement between theory and simulation. Apart from the behaviour in the immediate vicinity of the inlet and outlet, the lack of any streamwise variation is striking. We also compared the disturbance profiles with the eigenfunctions of the linear theory, again obtaining excellent agreement. Similar runs were made for channels with wholly compliant walls. In the interests of brevity these results are not shown, but they are as satisfactory as those shown in figure 4.

After carrying out extensive grid-dependency tests we found that generally 16 Chebychev polynomials were adequate for resolving all the features in the y-variations.

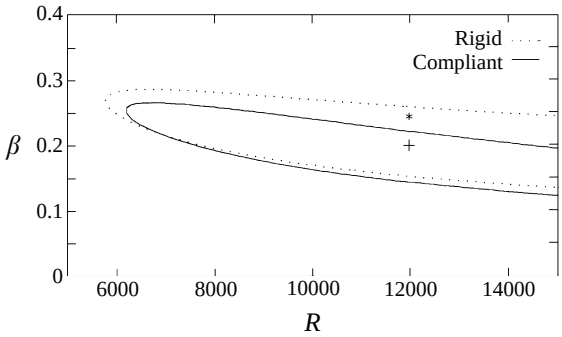

FIGURE 5. Neutral-stability curves for TS waves. The compliant-wall parameters are given in (4.1). The data points * and + denote the frequencies 0.24 and 0.2 respectively and both are at $R = 12\,000$.

For the simulations reported below we chose to use 32 Chebychev polynomials. The step size Δx required for the finite-difference discretization in the streamwise direction depended on the smallest wavelengths present. Generally 16 points per wavelength were required which corresponds to $\Delta x = 0.4$ for most of the simulations reported below. Longer flow domains were more demanding in this respect than shorter ones owing to the greater accumulation of phase error. For flow domains longer than those reported below smaller values of Δx were required. The size of the time step used in the simulations was dictated by the requirements of convergence rather than accuracy. The non-dimensional time steps used were typically $\Delta x/2$.

4. Results and discussion

4.1. *Results for TS frequency below cut-off*

For this simulation we set $R = 12\,000$ which is about twice the critical value for a rigid-walled channel. The wall parameters are

$$m = \tfrac{1}{3}, \quad T = 0, \quad d = 0, \quad B = 1.92 \times 10^7, \quad K = 4B. \tag{4.1}$$

These property values are quite similar to those attributed by Carpenter & Garrad (1985) to the original Kramer (1960) compliant coatings. The value of Reynolds number corresponds to a channel half-width of 1.5 mm and a centreline flow speed of 11 m s^{-1}, so there should be no reason why the wall properties could not be realized in practice.

The non-dimensional TS frequency chosen and the corresponding eigenvalues are

$$\beta = 0.24, \qquad \alpha = 1.03 - 0.0093\mathrm{i} \quad \text{(rigid)}, \qquad \alpha = 0.940 + 0.0109\mathrm{i} \quad \text{(compliant)}.$$

This corresponds to a case where the TS wave is amplified over the rigid surface and attenuated over the compliant wall. Figure 5 shows the location of the selected (β, R) values relative to the two neutral curves obtained from numerical solutions of the Orr–Sommerfeld equation. The selected value of β corresponds to a growth rate over the rigid wall which is about 60% of the maximum.

The streamwise development of the integrals of disturbance enstrophy (strictly defined as $\omega^2/2$) and kinetic energy,

$$\int_0^1 \omega^2 \mathrm{d}y \qquad \text{and} \qquad \frac{1}{2}\int_0^1 (u^2 + v^2)\mathrm{d}y,$$

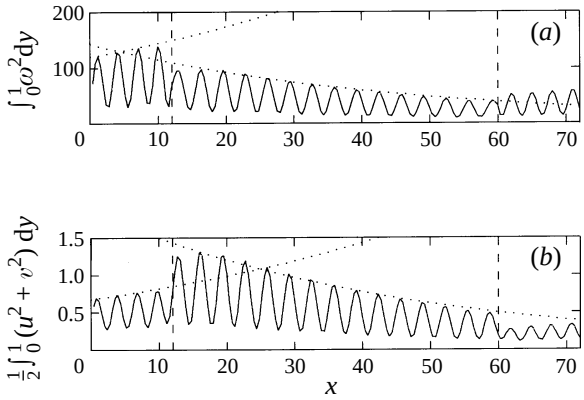

FIGURE 6. Streamwise development of the integrals of (*a*) disturbance enstrophy and (*b*) kinetic energy of a TS wave propagating along a channel containing a compliant section. The compliant-wall parameters are given in (4.1). $R = 12\,000$ and $\beta = 0.24$. The vertical broken lines indicate the locations of the panel edges here and in all subsequent figures of a similar type. · · · ·, The amplitude envelopes predicted by linear stability theory.

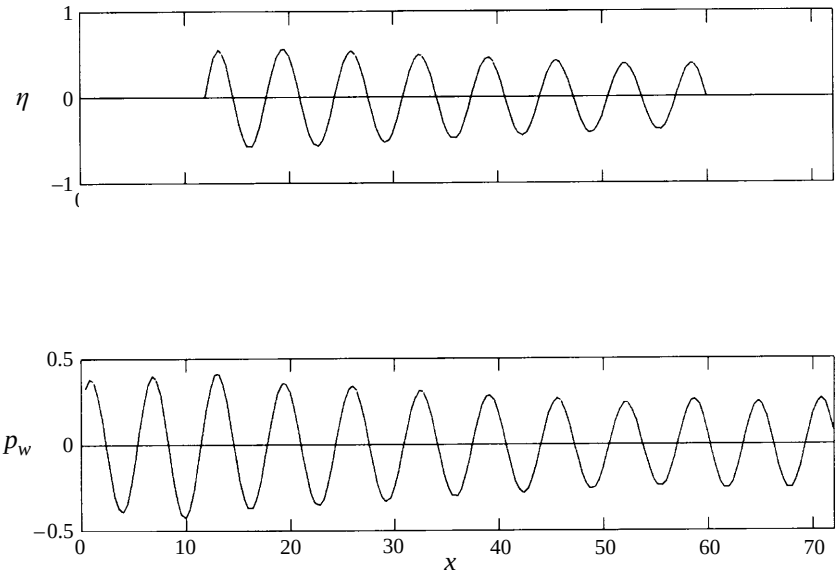

FIGURE 7. Streamwise variation of (*a*) wall displacement and (*b*) perturbation pressure for the case shown in figure 6.

are presented in figure 6 with the corresponding wall characteristics given in figure 7. It will be noticed that the apparent wavelength in figure 6 is half that in figure 7, this merely reflects the fact that the quantities in figure 6 are squares; the true TS wavelength is depicted in figure 7. Figure 8 shows both the streamwise and normal variations of u. It is an instantaneous representation obtained after the initial disturbance has reached the outlet of the domain. The response of the compliant panel obtained with this simulation is typical of cases where the TS frequency is below cut-off. The question of the cut-off frequency will be discussed in §4.3.

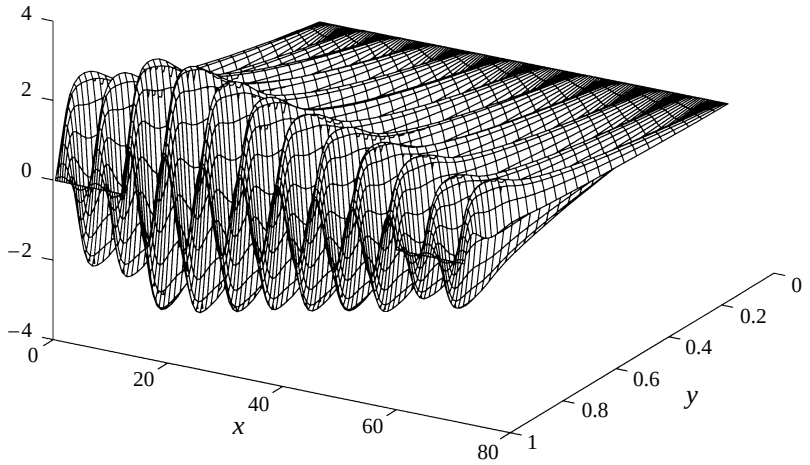

FIGURE 8. Spatial variation of the u-component of the fluid perturbation velocity for the case shown in figure 6. The grid lines of constant x correspond to the points used for the finite-difference discretization. The constant-y grid lines arise from evaluating the Chebyshev expansions for the flow variables at the Gauss–Lobatto points. $\Delta x = 0.4$ and the number of polynomials $N = 32$.

Three main features stand out in figures 6–8. First, plainly the adjustment of the TS wave to the change from rigid to compliant wall is very rapid. The dotted lines in figure 6 indicate the amplitude envelopes predicted by linear stability theory. The compliant panel extends from $x = 12$ to $x = 60$; and it can be seen from figure 6 that after the wave is incident on the leading edge of the compliant panel, within less than one wavelength its amplitude is falling exactly as predicted by the linear theory. Secondly, it is very striking how the kinetic energy and enstrophy change very abruptly at the edges of the compliant panel. The former rises and the latter falls at the leading edge and vice versa at the trailing edge. Lastly, it appears from figure 7 that the wall pressure is largely unaffected by the presence of the compliant panel.

The rapid changes in disturbance kinetic energy and enstrophy at the edges of the compliant panel are mainly due to rapid changes in the streamwise velocity component. The other velocity component, v, reaches its maximum value at the centreline where it is less influenced by the compliant wall. The u-component, on the other hand, as can be seen from figure 8, reaches its maximum near the wall where it is strongly influenced by the compliant wall. In particular, since u is no longer zero when the wall is compliant, there will be relatively greater kinetic energy near the wall and also $\partial u/\partial y$ will be reduced near the wall. This latter feature is responsible for the drop in vorticity at the leading edge.

4.2. *Analysis of the energy flux*

If the two linearized momentum equations for the disturbance are multiplied by u and v respectively, after some further manipulation the following governing equation for the disturbance kinetic energy is obtained:

$$\left(\frac{\partial}{\partial t} + U\frac{\partial}{\partial x}\right)\left[\tfrac{1}{2}(u^2+v^2)\right] + uv\frac{\mathrm{d}U}{\mathrm{d}y} + \frac{\partial(up)}{\partial x} + \frac{\partial(vp)}{\partial y} = \frac{1}{R}\left(\frac{\partial(u\omega)}{\partial y} - \frac{\partial(v\omega)}{\partial x} - \omega^2\right). \tag{4.2}$$

For time-periodic disturbances (4.2) may be averaged over a period (such averages are denoted by an overbar below) and then integrated across the channel half-width

to obtain the integral equation for the energy flux in the form

$$\frac{\mathrm{d}}{\mathrm{d}x}\Big[\overbrace{\int_0^1 \tfrac{1}{2}U(\overline{u^2}+\overline{v^2})\mathrm{d}y}^{(I)}+\overbrace{\int_0^1 \overline{up}\mathrm{d}y}^{(II)}+\overbrace{\frac{1}{R}\int_0^1 \overline{v\omega}\mathrm{d}y}^{(III)}\Big]$$
$$=\underbrace{\int_0^1 -\overline{uv}\frac{\mathrm{d}U}{\mathrm{d}y}\mathrm{d}y}_{\text{(i)}}-\frac{1}{R}\underbrace{\int_0^1 \overline{\omega^2}\mathrm{d}y}_{\text{(ii)}}-\underbrace{\overline{v_w p_w}}_{\text{(iii)}}+\underbrace{\frac{1}{R}\overline{u_w\omega_w}}_{\text{(iv)}}. \tag{4.3}$$

Equation (4.3) is similar to that derived by Morris (1976) in his study of the spatial stability of jets. He collected the terms (I) and (II) on the left-hand side and called them the integrated mechanical energy flux. Term (I) is the average disturbance kinetic energy being convected past a given streamwise location. Terms (II) and (III) are flow-work-type terms, being the rates of work done by the disturbances against the perturbation stresses across an imaginary boundary at the streamwise location in question. In practice, term (III) is invariably negligibly small.

Terms (i) and (ii) on the right-hand side of (4.3) are familar as the rates of energy production by the Reynolds stress and of viscous dissipation respectively. Term (iii) can be readily interpreted as the rate of irreversible work done to the wall by the disturbance pressure. Term (iv) poses some difficulty in interpretation. It is certainly not usually negligible and in all cases examined so far is negative. Carpenter (1990) identified it as an extra energy-removal term equivalent to additional viscous dissipation.

The streamwise variations of the various terms in (4.3) are depicted in figure 9. Noting the difference in scale between figures 9(*b*) and 9(*c*), it can be seen that, although term (i) – Reynolds-stress production – is of the same order of magnitude as the other main terms over the bulk of the panel, it completely dominates them at the panel edges. It is this large abrupt change in Reynolds-stress production at the leading and trailing edges which is responsible for the sharp changes in disturbance kinetic energy and enstrophy. A similar abrupt rise and fall is found in term (iii) – pressure work – in figure 9(*c*), although much smaller in magnitude than the Reynolds-stress production. The size of the Reynolds stress is determined by quite subtle phase differences between u and v, and sharp changes in the phase difference could be expected in the vicinity of the joins between rigid and compliant walls. It is clear from figure 9(*b*) that the leading edge exerts a considerable upstream influence since the Reynolds-stress production begins to rise steeply well before the wave reaches the join. Perhaps one can interpret the rise in energy as evidence of constructive interference between the incident and scattered waves. A similar, but destructive, interference appears to occur at the trailing edge.

4.3. *Approximate representation of wall response and cut-off frequency*

In the simulation described in §4.1 and §4.2 the wall response is completely dominated by the TS wave. It will be shown below that this is because the cut-off frequency is above the range of unstable TS frequencies. It is possible in some cases for the wall response to be strongly modified by flow-induced surface waves. For interpreting such complex responses it is helpful to formulate an approximate representation for the wall response.

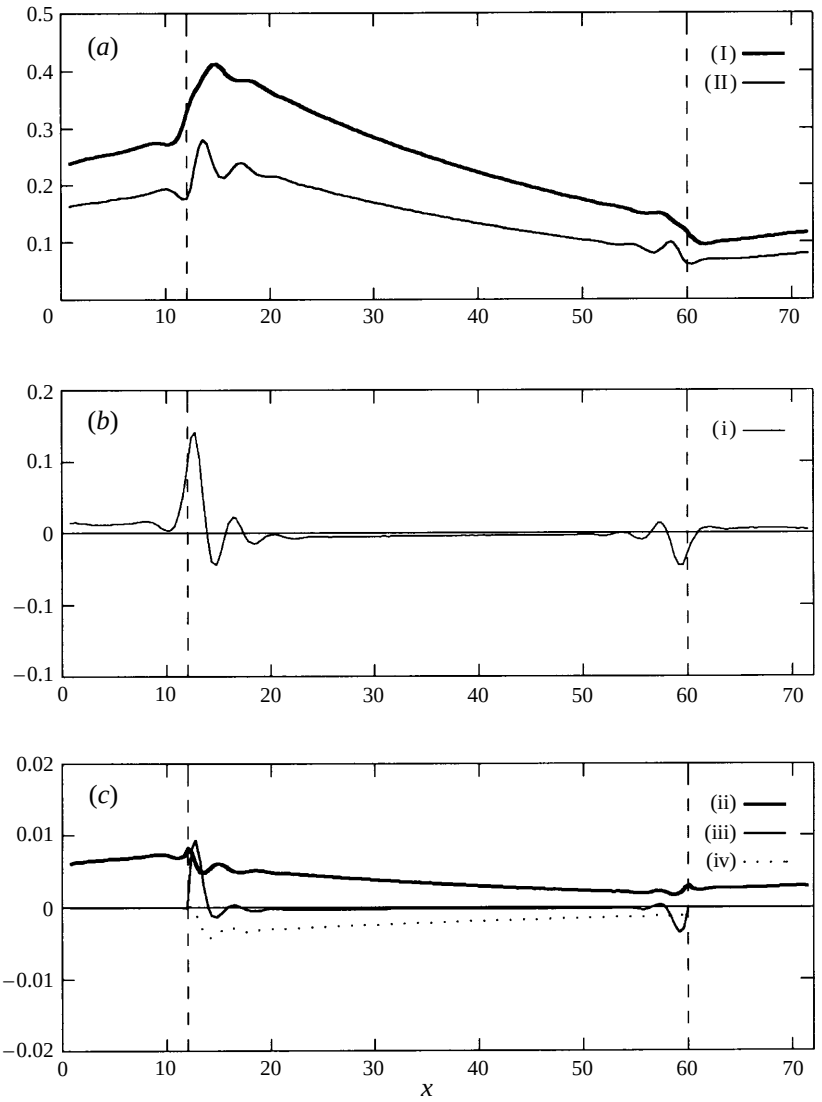

FIGURE 9. Streamwise variation of the terms in the energy flux equation (4.3) for the case shown in figure 6.

It will have been noted that in figure 7 the wall pressure appears to be very nearly unaffected by the presence of the joins between the rigid and compliant walls. To a reasonable approximation, therefore, over the compliant panel we could model the wall pressure as a superposition of Orr–Sommerfeld modes – the TS mode plus the various flow-induced surface modes of the Orr–Sommerfeld/compliant-wall eigensystem. Thus we take

$$p_w = \mathscr{R}\left\{\hat{p}_w \mathrm{e}^{\mathrm{i}\beta(t-t_0)}\right\}, \qquad \hat{p}_w = A_{ts}\mathrm{e}^{\mathrm{i}\alpha_{ts}x} + \sum_{i=1}^{n} A_i \mathrm{e}^{\mathrm{i}\alpha_i x}, \tag{4.4}$$

where t_0 is an arbitrary reference time , suffix ts denotes the TS mode, suffix i denotes one of n flow-induced modes, and A_{ts} and A_i are complex constants. When the wall

pressure is modelled by (4.4), it follows from the governing equation (2.5) for the wall motion that

$$\eta = \mathscr{R}\left\{\hat{\eta}\mathrm{e}^{\mathrm{i}\beta(t-t_0)}\right\}, \qquad \hat{\eta} = C_{ts}\mathrm{e}^{\mathrm{i}\alpha_{ts}x} + \sum_{i=1}^{n} C_i\mathrm{e}^{\mathrm{i}\alpha_i x} + \sum_{j=1}^{4} D_j\mathrm{e}^{\mathrm{i}\lambda_j x}, \tag{4.5}$$

where

$$C_{ts} = \frac{R^2 A_{ts}}{B\alpha_{ts}^4 + K - mR^2\beta^2}, \qquad C_i = \frac{R^2 A_i}{B\alpha_i^4 + K - mR^2\beta^2}.$$

The last term on the right-hand side of (4.4) represents the homogeneous solutions obtained by setting $\hat{p}_w = 0$ in the wall equation. In the present context these solutions are required in order to satisfy the boundary conditions (2.6) imposed at the edges of the compliant panel. Substituting from (4.4) into (2.5) and setting $p_w = 0$ shows that, in the case with no damping ($d = 0$) or tension ($T = 0$), the λ_j are given by the solution to

$$\lambda^4 = -\frac{K - m\beta^2 R^2}{B}.$$

Thus

$$\lambda_j = \begin{cases} \pm(1 \pm \mathrm{i})\gamma/\sqrt{2} & \text{if } K > m\beta^2 R^2 \\ \pm\gamma, \pm\mathrm{i}\gamma & \text{otherwise} \end{cases} \tag{4.6}$$

where

$$\gamma = \left(\frac{|K - m\beta^2 R^2|}{B}\right)^{1/4}.$$

The homogeneous solutions are thereby written as

$$\hat{\eta} = \begin{cases} \mathrm{e}^{\pm\gamma x/\sqrt{2}}\cos(\gamma x/\sqrt{2}), \quad \mathrm{e}^{\pm\gamma x/\sqrt{2}}\sin(\gamma x/\sqrt{2}) & \text{if } K > m\beta^2 R^2 \\ \mathrm{e}^{\pm\gamma x}, \quad \cos(\gamma x), \quad \sin(\gamma x) & \text{otherwise} \end{cases} \tag{4.7}$$

These solutions are illustrated in figure 3.

Evidently for free waves ($p_w = 0$) the cut-off frequncy is $\beta_0 = [K/(mR^2)]^{1/2}$. When a fluid flow is present the two solutions corresponding to (4.7) are strongly modified. Such solutions were termed flow-induced surface waves by Carpenter & Garrad (1986). To see what forms their dispersion relations take in particular cases, we can solve the Orr–Sommerfeld/compliant-wall eigensystem numerically. The dispersion relation for the case described in §4.1 is presented in figure 10. In this case the cut-off frequencies for free waves $\beta_0 = 1.26$ and unstable TS waves are found in the range $0.15 < \beta < 0.26$. It can be seen from figure 10 that the actual cut-off frequency is $\beta \simeq 0.37$ which is well above the frequency range for unstable TS waves, so it is not surprising that the compliant-panel response is dominated by the TS wave.

4.4. *Results for TS frequency above cut-off*

The wall parameters are now given by

$$m = \tfrac{1}{3}, \quad T = 0, \quad d = 0, \quad K = 1.92 \times 10^7, \quad B = 4K. \tag{4.8}$$

For these wall properties $\beta_0 = 0.63$, i.e. half the previous value. From figure 11 it can be seen that the dimensionless cut-off frequency is about 0.12 which is below the frequency range $0.13 < \beta < 0.20$ for unstable TS waves. The TS frequency and Reynolds number are the same as before. The relationship of the chosen pair of values (β, R) to the neutral curves obtained by numerical integration of the Orr–Sommerfeld equation is illustrated in figure 12.

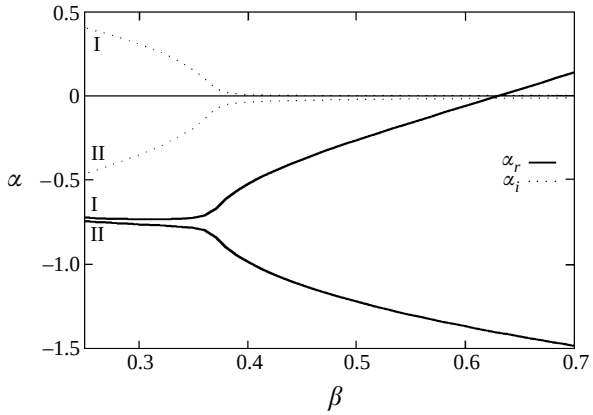

FIGURE 10. Variation of wavenumber with frequency for flow-induced surface waves for the case shown in figure 6.

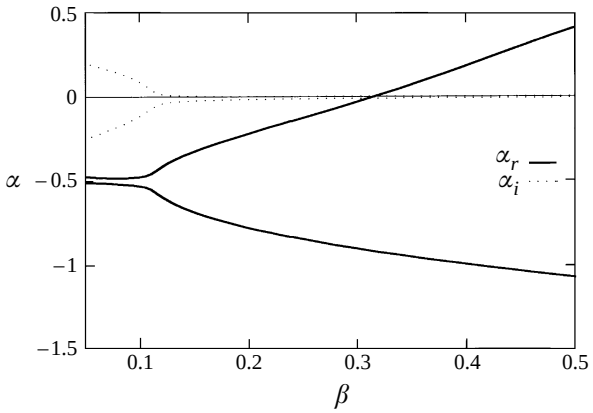

FIGURE 11. Variation of wavenumber with frequency for flow-induced surface waves for the compliant-wall properties given in (4.8) and $Re = 12\,000$.

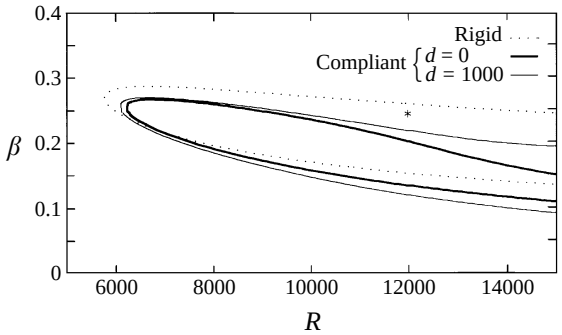

FIGURE 12. Neutral stability curves for TS waves. The compliant-wall parameters are as given in (4.8) unless specified otherwise. The data point marked by * corresponds to the simulation presented in figures 13–17.

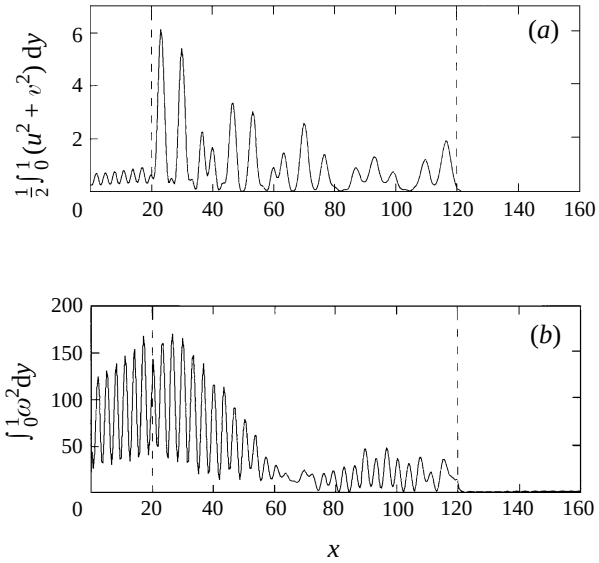

FIGURE 13. Instantaneous streamwise distribution of the integrals of (*a*) disturbance energy and (*b*) enstrophy. $\beta = 0.24$ and $Re = 12\,000$. Compliant wall properties are given in (4.8).

Plots of the streamwise variations of the integrals of disturbance kinetic energy and enstrophy are given in figure 13. The wall variables are plotted in figure 14 and the evolution of the *u*-profile along the channel is depicted in figure 15. All figures correspond to the same instant of time when the TS wave has propagated through and out of the computational domain. It is immediately apparent from the figures that the response of the compliant panel, which extends from $x = 20$ to $x = 120$, is very complex. Nonetheless, judging from the exceedingly low levels of the kinetic energy and enstrophy downstream of the compliant panel, it is very effective at suppressing TS waves. In fact, the level of disturbance energy is so low for $x > 120$ that it cannot be seen at all in figure 13. The level of enstrophy is also so low as to be barely discernible.

In order to make sense of the complex panel response we obtained power spectra by taking the discrete Fourier transform of the wall displacement, η, and vorticity, ω_w, at the wall for a single instant of time. The resulting spectra are plotted in figure 16. In each case we used only the data from the compliant panel $20 < x < 120$. Both spectra have been normalized to give the same maximum value. It is fairly clear from figure 16 that there are three components – a long-wave component and two others close together at higher wave-numbers. Each of these can be identified with an eigenmode of the Orr–Sommerfeld/compliant-wall eigensystem. The dotted lines plotted in figure 16 correspond to such eigenmodes, the wavenumbers being obtained from a global eigenvalue analysis. The three eigenvalues are

$$\alpha_1 = -0.15 + 0.00013\mathrm{i}, \quad \alpha_2 = -0.83 - 0.014\mathrm{i}, \quad \alpha_{ts} = 0.92 + 0.021\mathrm{i}. \tag{4.9}$$

The first two correspond to flow-induced surface waves and α_{ts} to the TS wave.

To help interpret the eigenmodes an approximate analysis is carried out. If time periodicity is assumed, it can be readily seen from the form (4.5) of the approximate representation (taking $n = 2$) that, at each streamwise location x_k, the complex amplitude of the wall displacement can be obtained from the simulation data

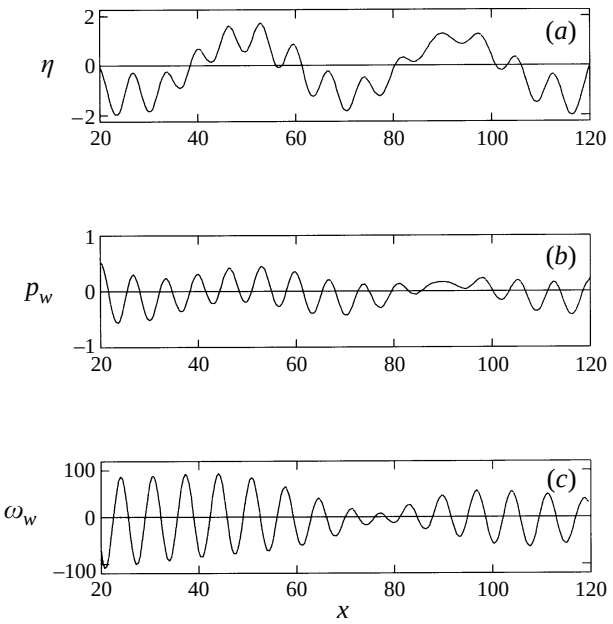

FIGURE 14. Streamwise variation of the wall-motion variables for the case shown in figure 13.

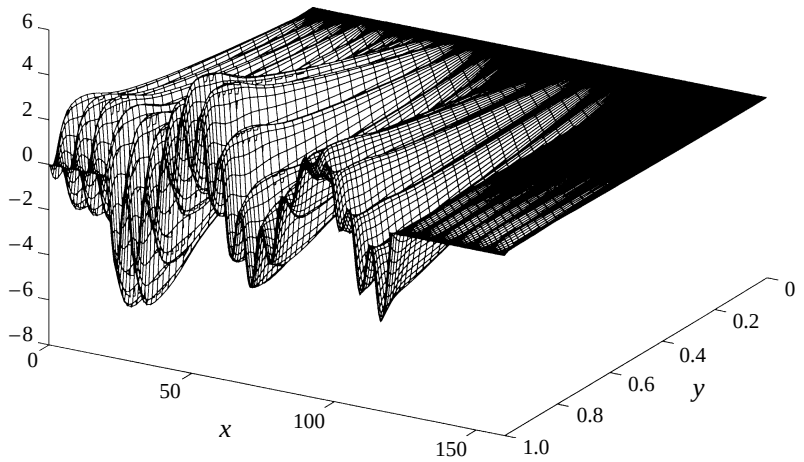

FIGURE 15. Spatial variation of the *u*-component of flow perturbation for the case shown in figure 13.

as follows:

$$\hat{\eta}_k = \left(\eta_k + \mathrm{i}\frac{1}{\beta}\frac{\partial \eta_k}{\partial t}\right)_{t_0}$$
$$= C_{ts}\mathrm{e}^{\mathrm{i}\alpha_{ts}x_k} + C_1\mathrm{e}^{\mathrm{i}\alpha_1 x_k} + C_2\mathrm{e}^{\mathrm{i}\alpha_2 x_k} + \sum_{j=1}^{4} D_j\mathrm{e}^{\lambda_j x_k}. \tag{4.10}$$

There are, of course, data for vastly more than seven values of x_k. Accordingly we can determine the seven complex constants C_{ts}, C_1, C_2 and D_j from a least-squares fit over all the data available. The agreement between the resulting representation (4.10)

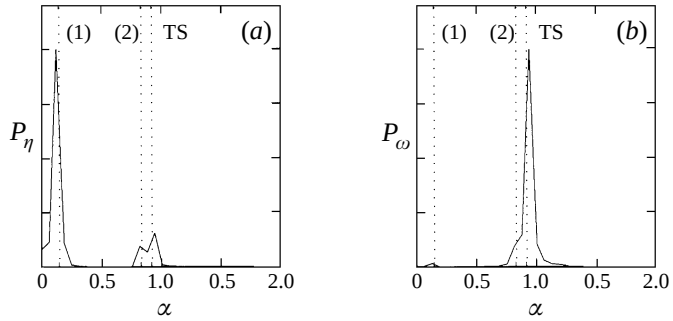

FIGURE 16. Power spectra obtained by analysing the instantaneous spatial distribution of (*a*) the wall displacement and (*b*) vorticity at the wall for the case shown in figure 13. The labels on the dotted vertical lines refer to eigenmodes of the coupled Orr–Sommerfeld/compliant-wall eigenproblem.

and the simulation data is almost perfect, suggesting that the representation contains all the essential elements.

Each component of the representation (4.10) is plotted separately in figure 17 for the wall displacement. The actual (or total) wall displacement is shown by the dotted curves. It will be seen that the contribution of the last term on the right-hand side of (4.10) – the so-called homogeneous solution – is only significant in the immediate vicinities of the panel edges. This is only to be expected from (4.7) since $\beta < \beta_0$ (the cut-off frequency for free waves). The close fit between (4.10) and the simulation data suggests that a theoretical solution to the problem under study could be developed based on the Orr–Sommerfeld equation and the equation of motion for the compliant wall. Further details of the analysis described in this section can be found in Davies (1995).

We turn now to the interpretation of the flow-induced eigenmodes 1 and 2. Although the phase velocities of modes 1 and 2 are both negative, the signs of the group velocities suggest that only mode 2 is upstream-propagating. This in itself is insufficient evidence because in a non-conservative medium the group velocity does not determine the direction of propagation unambiguously. Further evidence is to be found from simulations for cases with wall damping. These are not shown, but we can report that when wall damping is present mode 1 is strongly attenuated in the downstream direction becoming barely perceptible by the trailing edge. Likewise mode 2 is strongly attenuated in the upstream direction, becoming barely discernible at the leading edge. Observations of the transient behaviour as the TS wave propagates through the flow domain during the simulations also make plain where each mode originates. For example, mode 1 begins to propagate downstream from the leading edge of the panel before the TS wave has reached the trailing edge of the panel. Accordingly the eigenmodes can be interpreted as follows. Mode 1 is a downstream-propagating, relatively long, surface wave which is slowly attenuating. Mode 2 is an upstream-propagating surface wave with a wavelength very similar to the TS wave which decays much more rapidly than mode 1. Mode 1 could be regarded as resulting from the scattering of the TS wave at the leading edge of the panel. Mode 2 propagates upstream from the trailing edge of the panel and could be regarded as resulting from the partial reflection or scattering of the TS wave there.

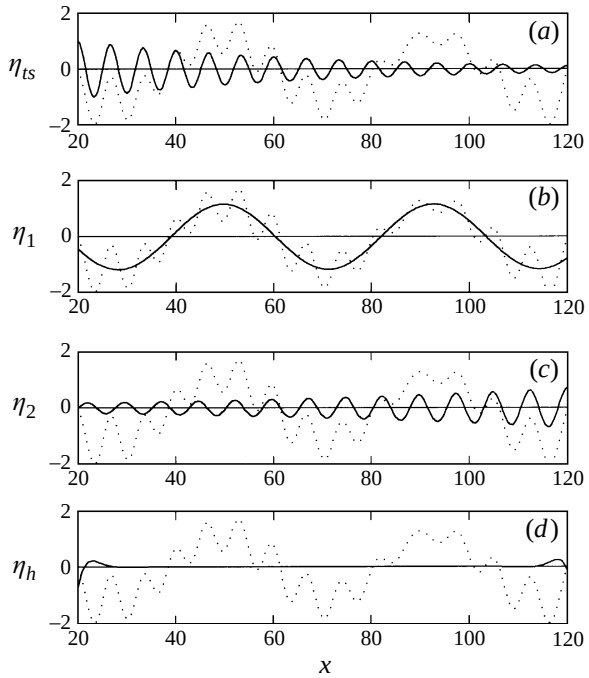

FIGURE 17. Components of wall displacement. (*a*) TS wave, (*b*) flow-induced surface wave with wavenumber α_1, (*c*) flow-induced surface wave with wavenumber α_2, and (*d*) component contributed by the homogeneous solution to the wall-motion equation. In each plot the total wall displacement is shown by the dotted curve.

4.5. *Some additional simulations*

4.5.1. *Partially stabilizing compliant panel*

The wall parameters in this case are identical to those used in §4.1 and given in (4.1), except that the frequency is lower at $\beta = 0.2$. This brings the TS wave into the unstable regime inside the neutral curve for the compliant surface – see figure 5. The TS wave now has a much reduced growth rate over the compliant panel rather than being attenuated. This state of affairs leads to some obvious differences from the results discussed in §4.1, but otherwise the physics is essentially unchanged. The TS wave still adjusts to the presence of the compliant wall very rapidly and the disturbance energy and enstrophy still exhibit the same sort of rapid changes at the panel edges.

4.5.2. *Damped compliant panel for TS frequency above cut-off*

For this simulation the wall parameters are the same (i.e. (4.8)) as used in §4.4 except that the damping coefficient $d = 1000$. (Note that the effective dimensionless damping coefficient is given by d/R). The corresponding neutral curve is plotted in figure 12. In this case the three eigenmodes which make up the main components of the wall motion are given by

$$\alpha_1 = -0.15 + 0.045\mathrm{i}, \quad \alpha_2 = -0.83 - 0.031\mathrm{i}, \quad \alpha_{ts} = 0.92 + 0.015\mathrm{i}.$$

The real parts are identical to those for the undamped simulation, but there is a strong stabilizing effect on the two flow-induced modes and the TS wave is slightly less damped.

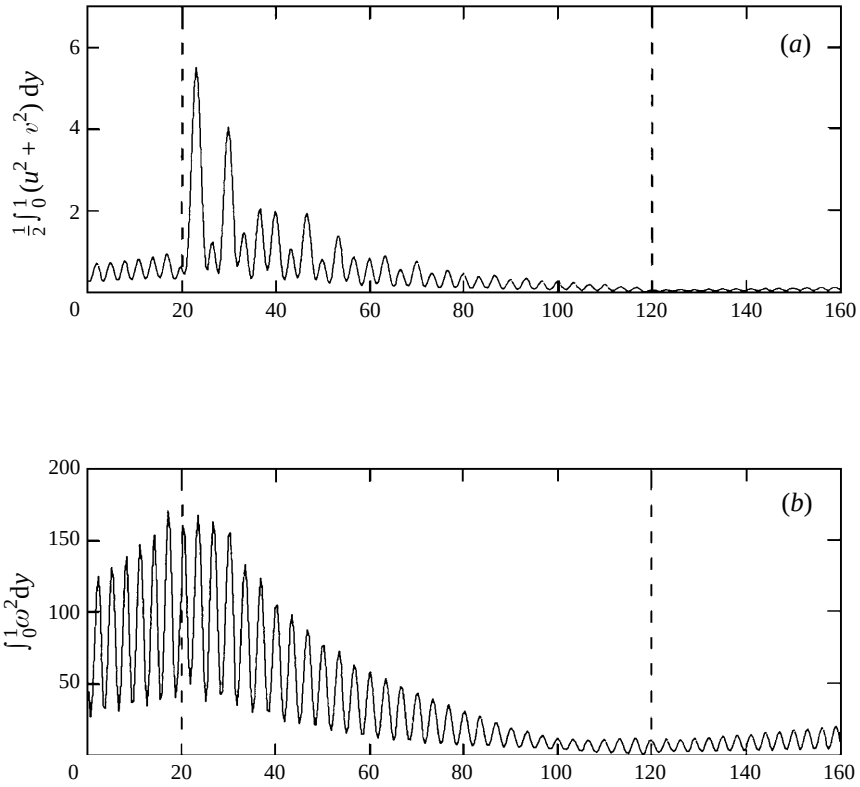

FIGURE 18. Instantaneous (*a*) disturbance kinetic energy and (*b*) enstrophy for a damped compliant panel; $d = 1000$ otherwise the wall and flow parameters are the same as for figure 13.

Figure 18 displays the integrals of disturbance energy and enstrophy. It can be seen that, again, there are large peaks in E in the vicinity of the panel's leading edge. There is a general decline in energy and enstrophy over the compliant panel, but the trailing edge cannot be distinguished so readily as in the undamped case. The spectra are not shown here, but it can be reported that mode 2 is now so weak that it cannot be discerned in the spectra. Nonetheless it probably does have a discernible effect near the panel's trailing edge where a slight rise in the amplitude of the enstrophy integral can be seen in figure 18(*b*).

4.5.3. *Very short compliant panels*

One of the practical motivations of the present work is to find out how short a compliant panel could be without losing its capability to suppress TS waves. Accordingly, we carried out the two simulations depicted in figure 19. In this case the panels extend from $x = 12$ to $x = 25.6$ and are about two TS wavelengths long. The frequency $\beta = 0.24$ and the Reynolds number $R = 12\,000$. The other properties for case (*a*) are as given in (4.1) and for case (*b*) as given in (4.8) except that $d = 1000$ in the latter case. Thus the TS frequency is below cut-off for case (*a*) and above for case (*b*). In both cases the panels are about two TS wavelengths long.

The time-averaged convected disturbance energy

$$E_c = \int_0^1 \tfrac{1}{2} U(\overline{u^2} + \overline{v^2}) \mathrm{d}y$$

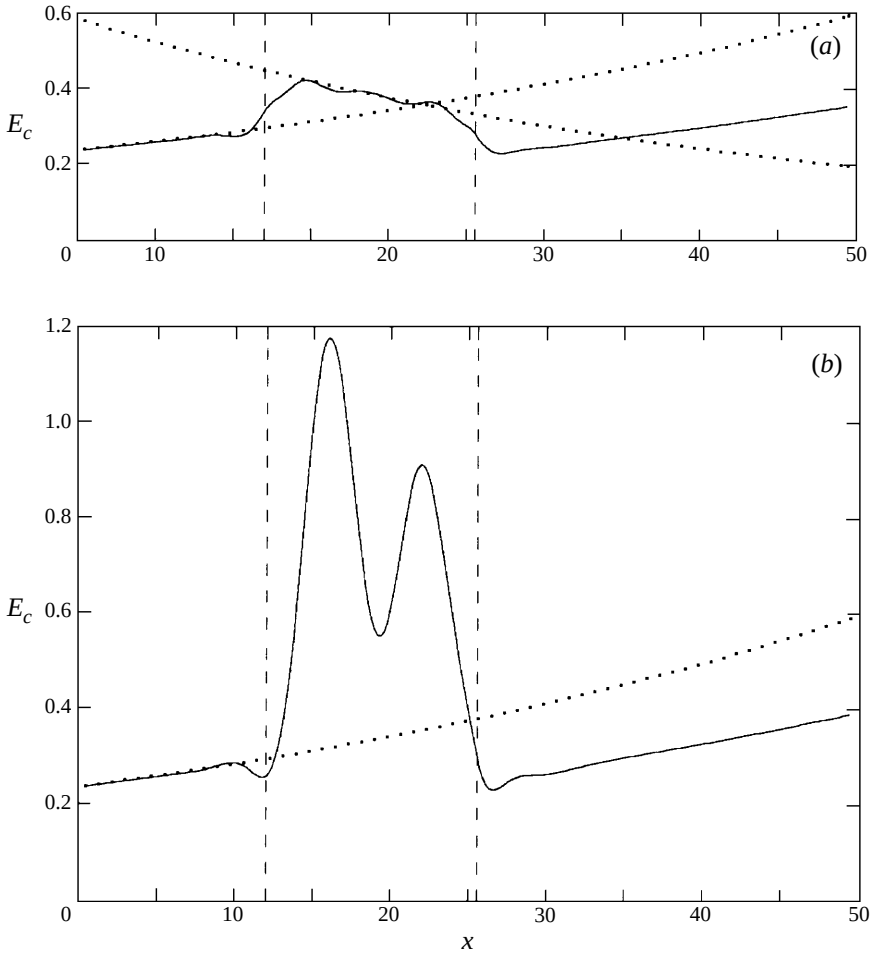

FIGURE 19. Streamwise distributions of the time-averaged convected disturbance energy for a TS wave passing over a very short compliant panel extending from $x = 12$ to $x = 25.6$. The other wall and flow parameters for (*a*) and (*b*) are the same as for figure 6 and figure 18 respectively.

is plotted in figure 19. It can be seen that the panel response for (*a*) is relatively simple and the the panel plainly suppresses the growth of TS waves. In case (*b*) the very large rise in convected disturbance energy at the leading edge and corresponding drop at the trailing edge of the panel obscures the evolution of the TS wave. Nonetheless to judge by the level of convected disturbance energy immediately downstream of the panel, it too retains its effectiveness in suppressing TS growth.

A few simulations were also carried out for very short compliant panels only a single TS wavelength long or even shorter. As may be expected in such cases the effects of the two compliant–rigid joins will dominate over any stabilizing effect similar to that exhibited by a longer panel. Moreover, not surprisingly, there was evidence of some kind of interference between the motions excited at each join. Interestingly, some simulations revealed that by using a very short compliant panel, it sometimes proved possible to obtain a larger reduction in disturbance amplitude than would have been achieved if instantaneous adaptation to the TS growth rate found over an

infinite compliant wall had been assumed at the joins. Plainly, this unexpected and novel stabilizing effect merits further investigation.

4.5.4. *Simulations for other values of Reynolds number and for panels with clamped ends*

The results presented above were all obtained for R=12 000. Simulations have been run at other Reynolds numbers (above the critical value) to confirm that these results are typical. Some simulations have also been obtained with clamped-end conditions imposed at the panel's leading and trailing edges. As would be expected the results show that the rapid changes at the leading and trailing edges are somewhat less severe with clamped ends, otherwise the flow physics is very similar.

5. Conclusions

Numerical experiments have been carried out on the evolution of two-dimensional Tollmien–Schlichting (TS) waves in a plane channel flow with part of the otherwise rigid wall replaced with a compliant panel. The numerical scheme is based on a novel velocity–vorticity formulation. The spatial discretization is achieved by means of a hybrid spectral/finite-difference approach, resulting in a very efficient and stable tridiagonal scheme. Stable converged solutions can be achieved taking full account of the wall inertia even for non-periodic temporal variation. The scheme copes successfully with the development of self-excited disturbances in the compliant panel and with strong upstream propagation of disturbances.

The simulations have led to the following main conclusions about the flow physics:

(i) Short compliant panels (even as short as one TS wavelength or less) retain an ability to suppress the growth of TS waves. Thus in a low-disturbance flow environment maintaining laminar flow at an indefinitely high Reynolds number may well be possible using suitably designed multiple-panel compliant walls. This assumes, of course, that no other instability mechanism comes into play.

(ii) Whether the TS wave is above or below the cut-off frequency of the compliant panel is an important factor in determining the form of the panel's response. When the TS frequency is below cut-off the panel's response is dominated by the TS wave, but for frequencies above cut-off the reponse is much more complex. The cut-off frequency in the presence of a shear flow is usually much lower than the value for free waves.

(iii) It is shown that when the TS frequency is above cut-off the wall motion can be very accurately described by a superposition of four components: the TS wave; a damped, flow-induced surface wave which propagates upstream from the trailing edge with a wavelength close to the TS one; a lightly damped, almost neutral, much longer, flow-induced surface wave that propagates downstream from the leading edge of the panel; and a local response at the panel edges that can be closely modelled by the solutions to the pressure-free equation of motion for the compliant wall. The three travelling-wave components are all eigenmodes of the coupled Orr–Sommerfeld/compliant-wall eigensystem while the fourth component takes a very simple analytical form. This suggests that a theoretical solution to the problem could be developed based on the Orr–Sommerfeld equation.

(iv) The panel edges exert a strong upstream influence. This either manifests itself in a localized fashion near the leading edge or over a much greater distance in the form of the upstream-propagating wave mentioned in (iii).

(v) The integrals of disturbance kinetic energy and enstrophy exhibit very rapid streamwise change in the vicinity of the panel edges. The energy integral always rises sharply at the leading edge and falls at the trailing edge. The opposite is true for the enstrophy integral. A study of the various energy flux terms shows that this behaviour is associated with a rapid rise in the energy production by the Reynolds shear stress at the leading edge followed by the reverse at the trailing edge. There is also a much smaller rapid rise in the work done by the pressure force near the leading edge. These rapid streamwise variations would tend to increase the receptivity of boundary layers to free-stream disturbances. Another, possibly relevant, adverse effect of rapid streamwise variations was revealed in recent wind-tunnel experiments on boundary-layer instability described by Medeiros & Gaster (1996) and Healey (1995). They showed that rapid variations in amplitude can enhance nonlinear breakdown. Neither of these effects were investigated here, but they could reduce some of the benefits of using short panels.

(vi) The observations in the items (i) to (v) above pertain to undamped compliant walls. The picture is not greatly different when damping is included. Its main effect is to attenuate both the surface waves.

The work described in this paper was undertaken with the support of MTD Ltd. and EPSRC through the award of a research grant.

REFERENCES

Belanger, F., De Langre, E., Axisa, F., Païdoussis, M. P. & Mateescu, D. 1994 Dynamics of coaxial cylinders in laminar annular flow by simultaneous integration of the Navier-Stokes and structural equations. *J. Fluids Struct*. **8**, 747–770.

Bertolotti, F. P., Herbert, Th. & Spalart, P. R. 1992 Linear and nonlinear stability of the Blasius boundary layer. *J. Fluid Mech.* **242**, 441–474.

Bridges, T. J. & Morris, P. J. 1984 Differential eigenvalue problems in which the parameter appears nonlinearly. *J. Comput. Phys.* **55**, 437–460.

Canuto, C., Hussaini, M.Y., Quarteroni, A. & Zang, T. A. 1988 *Spectral Methods in Fluid Dynamics.* Springer.

Carpenter, P. W. 1990 Status of transition delay using compliant walls. In *Viscous Drag Reduction in Boundary Layers* (ed. D. M. Bushnell & J. N. Hefner), pp. 79–113. AIAA.

Carpenter, P. W. 1993 The optimization of multiple-panel compliant walls for delay of laminar–turbulent transition. *AIAA J.* **31**, 1187–1188.

Carpenter, P. W. & Garrad, A. D. 1985 The hydrodynamic stability of flow over Kramer-type compliant surfaces. Part 1. Tollmien–Schlichting instabilities. *J. Fluid Mech.* **155**, 465–510.

Carpenter, P. W. & Garrad, A. D. 1986 The hydrodynamic stability of flow over Kramer-type compliant surfaces. Part 2. Flow-induced surface instabilities. *J. Fluid Mech.* **170**, 199–232.

Carpenter, P. W. & Morris, P. J. 1990 The effect of anisotropic wall compliance on boundary–layer stability and transition. *J. Fluid Mech.* **218**, 171–223.

Davies, C. 1995 Evolution of Tollmien–Schlichting waves over a compliant panel. PhD thesis, University of Warwick, UK.

Dixon, A. E., Lucey, A. D. & Carpenter, P. W. 1994 The optimization of viscoelastic walls for transition delay. *AIAA J.* **32**, 256–267.

Domaradzki, J. A. & Metcalfe, R. W. 1987 Stabilization of laminar boundary layers by compliant membranes. *Phys. Fluids* **30**, 695–705.

Drazin, P. G. & Reid, W. H. 1981 *Hydrodynamic Stability*. Cambridge University Press.

Duncan, J. H., Waxman, A. M. & Tulin, M. P. 1985 The dynamics of waves at the interface between a viscoelastic coating and a fluid flow. *J. Fluid Mech.* **158**, 177–197.

Fasel, H. 1976 Investigation of the stability of boundary layers by a finite difference model of the Navier-Stokes equations. *J. Fluid Mech.* **78**, 355–383.

Fasel, H. 1980 Recent developments in the numerical solution to the Navier-Stokes and hydrodynamic stability problems. In *Computational Fluid Dynamics*, pp. 167–280. Hemisphere.

Fasel, H. & Konzelmann, U. 1990 Non-parallel stability of a flat plate boundary layer using the complete Navier–Stokes equations. *J. Fluid Mech.* **221**, 311–347.

Fasel, H., Rist, U. & Konzelmann, U. 1990 Numerical investigation of the three-dimensional development in boundary-layer transition. *AIAA J.* **28**, 29–37.

Gaster, M. 1987 Is the dolphin a red herring? In *IUTAM Symp. on Turbulence Management and Relaminarisation, Bangalore, India* (ed. H. W. Liepmann & R. Narasimha), pp. 285–304. Springer.

Gatski, T. B. 1991 Review of incompressible fluid flow computations using the vorticity-velocity formulation. *Appl. Numer. Maths* **7**, 227–239.

Gilbert, N. & Kleiser, L. 1986 Subcritical transition to turbulence in channel flow. In *Direct and Large Eddy Simulation of Turbulence* (ed. U. Schumann & R. Friedrich), pp. 1–18. Braunschweig: Vieweg.

Grotberg, J. B. 1994 Pulmonary flow and transport phenomena. *Ann. Rev. Fluid Mech.* **26**, 529–571.

Healey, J. J. 1995 A new boundary layer resonance enhanced by wave modulation: theory and experiment. *J. Fluid Mech.* **304**, 231–262.

Henry, F. S. & Collins, M. W. 1996 Numerical predictions of flow in a model compliant artery. Submitted to *J. Fluids Struct*.

Kamm, R. D. 1987 Flow through collapsible tubes. In *Handbook of Bio-engineering* (ed. R. Skalak & S. Chien), pp. 23.1–23.19. McGraw-Hill.

Kamm, R. D. & Pedley, T. J. 1989 Flow through collapsible tubes: a brief review. *Trans. ASME: J. Biomech. Engng* **111**, 177–179

Kendall, J. M. 1970 The turbulent boundary layer over a wall with progressive waves. *J. Fluid Mech.* **41**, 259–281.

Kloker, M., Konzelmann, U. & Fasel, H. 1993 Outflow boundary conditions for spatial Navier-Stokes simulations of transition boundary-layers. *AIAA J.* **31**, 620–628.

Kramer, M. O. 1960 Boundary–layer stabilization by distributed damping. *J. Am. Soc. Naval Engrs* **72**, 25–33.

Lucey, A. D., Cafolla, G. J. & Carpenter, P. W. 1997 Numerical simulation of a boundary-layer flow interacting with a passive compliant boundary. In *Proc. 15th Intl Conf. on Numerical Methods in Fluid Dynamics, Monterey, CA*, 24–28 June, 1996. *Lectures in Notes Physics*. Springer (to appear).

Lucey, A. D. & Carpenter, P. W. 1992 A numerical simulation of the interaction of a compliant wall and inviscid flow. *J. Fluid Mech.* **234**, 121–146.

Lucey, A. D. & Carpenter, P. W. 1993*a* On the difference between the hydroelastic instability of infinite and very long compliant panels. *J. Sound Vib.* **163**, 176–181.

Lucey, A. D. & Carpenter, P. W. 1993*b* The hydroelastic stability of three-dimensional disturbances of a finite compliant wall. *J. Sound Vib.* **165**, 527–552.

Lucey, A. D. & Carpenter, P. W. 1995 Boundary layer instability over compliant walls: Comparison between theory and experiment. *Phys. Fluids* **7**, 2355–2363.

Luo, X. Y. & Pedley, T. J. 1995 A numerical simulation of steady flow in a 2-D collapsible channel. *J. Fluids Struct.* **9**, 149–174.

Luo, X. Y. & Pedley, T. J. 1996 A numerical simulation of unsteady flow in a 2-D collapsible channel. *J. Fluid Mech.* **314**, 191–225.

Medeiros, A. F. & Gaster, M. 1996 The non-linear behaviour of modulated Tollmien–Schlichting waves. In *IUTAM Symp. on Nonlinear Instability and Transition in Three-Dimensional Boundary Layers, Manchester, UK* (ed. P. W. Duck & P. Hall), pp. 197–206. Kluwer.

Metcalfe, R. W., Battistoni, F., Ekeroot, J. & Orszag, S. A. 1991 Evolution of boundary layer flow over a compliant wall during transition to turbulence. In *Boundary Layer Transition and Control, Cambridge UK*, pp. 36.1–36.14. Royal Aeronautical Society.

Morris, P. J. 1976 The spatial viscous instability of axisymmetric jets. *J. Fluid Mech.* **77**, 511–529.

Morse, P. M. & Ingard, K.U. 1968 *Theoretical Acoustics*. McGraw-Hill.

Pedley, T. J. 1992 Longitudinal tension variation in collapsible channels: a new mechanism for the breakdown of steady flow. *Trans. ASME: J. Biomech. Engng* **114**, 60–67.

Rast, M. P. 1994 Simultaneous solution of the Navier-Stokes and elastic membrane equations by a finite element method. *Intl J. Numer. Meth. Fluids* **19**, 1115–1135.

Schlichting, H. 1979 *Boundary Layer Theory* 7th Edn. McGraw-Hill.

Skalak, R., Özkaya, N. & Skalak, T.C. 1989 Biofluid mechanics. *Ann. Rev. Fluid Mech.* **21**, 167–204.

Wray, A. & Hussaini, M. Y. 1984 Numerical experiments in boundary-layer stability. *Proc. R. Soc. Lond.* A **392**, 373–389.

Yeo, K. S. 1988 The stability of boundary-layer flow over single- and multi-layer viscoelastic walls. *J. Fluid Mech.* **196**, 359–408.